Probing gravity with redshift-space distortions:
Effects of tracer bias and sample selection

Jorge Enrique García-Farieta[ORCID],[*] Wojciech A. Hellwing[ORCID],[†] Suhani Gupta[ORCID],[‡] and Maciej Bilicki[ORCID][§]

Center for Theoretical Physics, Polish Academy of Sciences, Al. Lotników 32/46, 02-668 Warsaw, Poland

We investigate clustering properties of dark matter halos and galaxies to search for optimal statistics and scales where possible departures from general relativity (GR) could be found. We use large N-body cosmological simulations to perform measurements based on the two-point correlation function (2PCF) in GR and in selected modified gravity (MG) structure formation scenarios. As a test bed, we employ two popular beyond-GR models: $f(R)$ gravity and the normal branch of the Dvali-Gabadadze-Porrati (nDGP) braneworld. We study a range of simulated halo and galaxy populations and reveal a noticeable MG signal in the monopole and quadrupole moments of the redshift-space 2PCF and in the so-called clustering wedges. However, once expressed in terms of the linear distortion parameter β, the statistical significance of these signals largely diminishes due to a strong degeneracy between MG-enhanced clustering and modified tracer bias. To circumvent this, we consider statistics less dependent on the bias: relative clustering ratios. We generalize the monopole ratio proposed in earlier work to multipole moments and clustering wedges and introduce a new estimator of the β parameter. The clustering ratios we extract foster noticeable differences between MG and GR models, reaching a maximum deviation of 10% at 2σ significance for specific variants of $f(R)$ and the nDGP. We show that such departures could be measured for β if nonlinear effects at intermediate scales are correctly modeled. Our study indicates that the clustering ratios give great promise to search for signatures of MG in the large-scale structure. We also find that the selection of an optimal tracer sample depends on a particular statistics and gravity model to be considered.

I. INTRODUCTION

The standard cosmological model, lambda-cold dark matter (ΛCDM), assumes general relativity (GR) as a description of gravity on all scales and at all times. A simple parametrization of ΛCDM in terms of just six quantities provides an excellent fit to numerous observational data of various kinds collected over decades [e.g., [1–6]], but we are left with a puzzling outcome. According to ΛCDM, the Universe, for the most of its evolution, is dominated by dark components of yet unknown physical nature: collisionless cold dark matter (DM), constituting most of the cosmic mass, and a cosmological constant as the source of dark energy that causes the observed acceleration of the cosmic expansion. The existence of the cosmological constant, commonly associated to a negative-pressure fluid, would have profound implications for fundamental physics, however, there is no compelling direct evidence for it yet [7–10].

The urgent need to explain the physical mechanism behind the cosmic acceleration and, more generally, the nature of the dark sector, gives motivation to investigate the validity of GR on cosmological scales and to consider models of gravity beyond Einstein's theory. Such alternative frameworks may postulate, for instance, modifications in the theory of gravity on cosmological scales, but to be viable they must be consistent with experiments. In particular, they need to predict the same observationally well-constrained expansion history as ΛCDM and, at the same time, have to pass the stringent local and high-energy tests of gravity, where GR has been shown to work very well [11–15]. Among the proposed modifications of GR that we will refer to as "modified gravity" (MG), sometimes referred to in the literature as Extended Theories of Gravity (for a detailed review see, e.g., [16]), the models based on $f(R)$ gravity and braneworld stand out because of their generality and rich phenomenology [17–20].

The large-scale structure of the Universe is one of the richest sources of cosmological information, available chiefly in the clustering of matter tracers. Clustering is an important probe of the underlying cosmological model in which cosmic structures evolve, and therefore, it can be used to test the gravity theory [21–26]. In fact, the growth rate of structures, a parameter that describes the time

---
[*]jorge@cft.edu.pl
[†]hellwing@cft.edu.pl
[‡]gupta@cft.edu.pl
[§]bilicki@cft.edu.pl

103524-1

evolution of matter overdensities, can be used to differentiate from ΛCDM those alternative MG models that otherwise have expansion history compatible to GR.

One of main statistical measures of clustering is the two-point correlation function (2PCF), or the power spectrum, its equivalent in the Fourier space. In this work we study the former of these statistics, with the main focus on the redshift space, in which a wealth of observations are made. We also investigate the tracer (galaxy and halo) bias, which is notoriously difficult to model and constitutes one of the main sources of systematic errors plaguing the derivations of cosmological parameters from galaxy redshift surveys [e.g., [27,28]].

A specific feature suitable to test gravity models using the galaxy distribution and, in particular, to measure the growth rate, is redshift-space distortions (RSD) [29,30]. These appear naturally in observations due to radially-projected peculiar velocities that are a direct consequence of the growth of structure and the gravitational interaction. RSD induce anisotropy in the observationally derived 2PCF and are directly accessible in surveys that provide sky positions and spectroscopic redshifts of the tracers.

In view of the forthcoming and planned redshift surveys offering much better statistics than possible so far [31,32], challenges arise in using RSD for robust cosmological constraints and reliable tests of gravity. In particular, modeling of RSD is a paramount task, but not always successful, in the estimation of the growth factor. Several RSD models commonly extended from the linear theory formalism have proven to perform well at large scales, however, exploration of the nonlinear regime, where the most cosmological information is contained, is crucial in testing gravity. The commonly used modeling generally fails to describe accurately the full dynamics of the tracers at nonlinear and weakly nonlinear scales [33,34]. Over time, more elaborated approaches than the standard linear dispersion model have been proposed based on different perturbation theory schemes [22,35–37]. In general, however, these more advanced approaches were not designed for, nor thoroughly tested on, alternative gravity scenarios. Only in recent years some progress in that aspect has been made, but the developments apply only to RSD of a smooth DM component, rather than to the full clustering of biased tracers and, furthermore, they are available only for some selected MG models [23,38–41].

The difficulties described above are often combated thanks to high-resolution N-body simulations, which by construction can probe deeply into the nonlinear regime. They thus provide both a means to test the performance of various RSD models and a way to better understand the galaxy biasing and velocities in the full nonlinear regime. Running and employing N-body simulations for RSD studies has, therefore, become routine practice in the field. However, high-resolution and fully nonlinear simulations of MG are much more computationally expensive—by a

factor of a few to even one order of magnitude—than the same resolution ΛCDM setup. As a consequence, MG simulations of volumes and resolutions sufficient for galaxy and halo RSD studies are usually prohibitively expensive. However, with the recent advent of improved and accelerated algorithms to solve for the additional MG physics, suitable N-body simulations became available for beyond-GR models [e.g., [42–46]]. Thanks to this, systematic studies comparing RSD signals and models in ΛCDM vs MG scenarios have become possible [e.g., [47–51]].

In this paper, we investigate DM halo and galaxy clustering and the underlying growth rate of cosmic structures in two beyond-GR scenarios: $f(R)$ and the normal branch of the Dvali-Gabadadze-Porrati (nDGP), and compare them with ΛCDM. For that purpose we employ a set of mock catalogs with number densities characteristic to those accessible in today's and the near-future spectroscopic redshift surveys, such as SDSS (Sloan Digital Sky Survey), BOSS (Baryon Oscillation Spectroscopic Survey) or DESI (Dark Energy Spectroscopic Instrument). These catalogs are based on a suite of state-of-the-art N-body simulations: the Extended Lensing Physics using Analytic ray Tracing project (ELEPHANT; [51,52]). Our study is a continuation and extension of earlier works that employed these simulations. In Ref. [53] DM halo populations of ΛCDM and $f(R)$ models were studied with a novel clustering statistic called the halo clustering ratio $\mathcal{R}$. That analysis indicated that the clustering ratio has potential of discriminating between standard gravity and the $f(R)$ models, especially those with a milder departure from GR. More recently, Ref. [54] investigated the clustering of ELEPHANT mock galaxies using multipole moments and clustering wedges of the 2PCF. Their results confirm that the RSD measurements can help to distinguish between different gravity models. However, they highlight that the distortion parameter that obtained β with the linear RSD model is significantly underestimated for all the MG models they studied.

In our work we go beyond the scope of these previous studies in a number of important aspects. First, from the N-body simulations we use mock galaxies, as well as three different halo populations, which allows us to study the importance of tracer sampling density in searching for MG signatures and analyze the behavior of the linear bias in various gravity models. Second, we generalize the definition of the relative clustering ratio proposed in Ref. [53] to the multipole moments and clustering wedges and introduce a new estimator based on this ratio to constrain the linear distortion parameter β from redshift-space anisotropies. Although we only use the linear theory to model RSD, the new estimator is powerful enough to expose the impact of the scale at which measurements are made on recovering β. We also shed light on the degeneracy between the tracer bias and the growth rate, both encoded in the β parameter. Finally, we alleviate the issue addressed in [54] related to the efficacy of the linear model to recover the

linear distortion parameter. We show that an appropriate estimator of β based on linear theory can successfully recover its true value in the linear regime.

The paper is organized as follows: in Sec. II we briefly describe the cosmological models studied here. In Sec. III we present the set of N-body simulations that have been employed in the analysis and provide details on the selected DM halo populations, as well as the simulated galaxy sample. In Sec. IV we discuss the estimators used to characterize the clustering measurements of different samples in both the real and redshift space. In Sec. V we present the results and analysis of the clustering measurements for different halo populations and the galaxy sample; we also study the linear halo and galaxy bias in that Section. Then, in Sec. VI we introduce the estimator for relative clustering of multipole moments and wedges of the 2PCF and discuss the results obtained for our samples. Finally, in Sec. VII we conclude and discuss the implications of our findings.

II. MODIFIED GRAVITY MODELS

Beyond-GR alternatives to the ΛCDM cosmological model are numerous (see, e.g., the reviews [55,56]), but numerous are also the problems they have to struggle with. Some of these MG models are plagued with theoretical instabilities, and all of them obviously have to face observational constraints, which often requires fine-tuning of model parameters. One particularly simple extension of GR is by including a single scalar field φ in the Einstein-Hilbert Lagrangian, which sources gravity. However, when coupled to matter, the scalar field gives rise to an additional gravitational force—often referred to as the "fifth force." Such a fifth force can be quantified by $\gamma \equiv |F_5|/F_N$, where F_N is the standard Newtonian gravitational force that we obtain in the weak-field limit of GR. Several experiments [e.g., [57,58]] have constrained $\gamma \ll 1$ on Earth, in the Solar System, in neutron star binaries, and merging black holes. This leaves two possibilities: either there is no room to deviate from GR on all scales, i.e., $\gamma \equiv 0$, or γ is not a constant but instead varies in space (and possibly time). The latter scenario can be relatively easily realized if the fifth force arises due to the propagation of extra degrees of freedom of a dynamical field that varies in space and time. Models where this is the case are dubbed "screened" MG models since the fifth force is screened in high-curvature or high-potential regions.

In this work we study two classes of MG models: the $f(R)$ gravity of Hu-Sawicki formulation [59] and the nDGP braneworld gravity. In the former, the MG phenomenology arises from a generalization of the Ricci's scalar R in the Einstein-Hilbert action to a functional of it $f(R)$, and the fifth force is manifested due to an extra degree of freedom of the scalaron field of R. In the latter, the so-called nDGP model [60], the fifth force is a manifestation of an extra degree of freedom that is due to the bending of a four-dimensional brane in the five-dimensional bulk space-time.

In both cases, the arising fifth force can be modeled as a gradient of an underlying phenomenological scalar field.

We choose the $f(R)$ and the nDGP gravity models since they constitute a very good test suite for a wider class of MG theories. This is because most of the viable MG models can be divided into two general categories, depending on the physical mechanism of the fifth-force screening they invoke. The screening can be either "environment dependent" or "object-mass dependent." The former responds to the local value of the gravitational potential, and in the latter (also called the Vainshtein mechanism [61,62]), the effectiveness of the screening is usually moderated by the local curvature of a given region of space. What is also essential here is that the two classes of MG models we consider pass the stringent tests from the first kilonova gravitational wave event of GW170817 [63]. Below we give a short description of the specific formulations and settings of these two models. From the point of view of the statistics and observables studied in this paper, the most important characteristic of our models is that we choose specific formulations of $f(R)$ and the nDGP gravity theories that follow closely the ΛCDM expansion history. Thus, the first nonzero physical effect that emerges from their extra degrees of freedom is imprinted in modified history of the growth of structures.

A. Dvali-Gabadadze-Porrati model

The Dvali, Gabadadze & Porrati (DGP) model [60] is inspired by string theory and assumes the existence of a $4 + 1$-dimensional Minkowski space, within which the ordinary $3 + 1$-dimensional Minkowski space is embedded. In other words, the DGP model is one of the possible braneworld cosmology models, where the Universe is described by a 4D-brane which is embedded in a higher-dimensional space-time called the bulk [64]. In this respect, the so-called normal branch DGP (nDGP) gravity is a natural extension of the DGP model [60,65] that provides an explanation why the force of gravity is much weaker compared to the other fundamental forces [20]. This is possible because fundamental matter particles are assumed to be confined to the brane, while gravity can propagate through the extra spatial dimension(s).

The nDGP model introduces a free parameter, the so-called crossing-over scale r_c. It characterizes the scale at which the four-dimensional gravity of the brane "leaks out" to the five-dimensional bulk space-time. This scale is simply obtained as half of the ratio of the five-dimensional Newton constant $G^{(5)}$ to the usual four-dimensional one, denoted here simply as G:

$$r_c = \frac{1}{2}\frac{G^{(5)}}{G}.$$ (1)

The crossing-over scale limits the size of the fundamental perturbation of the embedded 4D-brane (i.e., the maximum

bending mode), and the extra degree of freedom of the brane can be expressed by a free scalar field φ. On the linear level, this translates to a maximum enhancement of the growth rate of structures, compared to the usual ΛCDM background. In the limit where the time derivatives of this new scalar field are negligible compared to its spatial derivatives, that is in the so-called quasistatic limit [65], the model admits a modified Poisson equation for gravity

$$\nabla^2 \Psi = 4\pi G a^2 \rho \delta + \frac{1}{2}\nabla^2 \varphi, \tag{2}$$

where Ψ is the classical Newtonian potential, G is the 4D Newton constant, a is the scale factor, ρ is the matter background density with its local density contrast δ, and finally, φ is the scalar field describing the extra degrees of freedom of the model. The new scalar field obeys its own equation of motion [42,66,67]

$$\nabla^2 \varphi + \frac{r_c^2}{3\mathcal{B}(a)a^2}[(\nabla^2\varphi)^2 - (\nabla_i\nabla_j\varphi)(\nabla^i\nabla^j\varphi)]$$
$$= \frac{8\pi G a^2}{3\mathcal{B}(a)}\rho\delta. \tag{3}$$

The new function $\mathcal{B}(a)$ is defined as

$$\mathcal{B}(a) = 1 + 2Hr_c\left(1 + \frac{\dot{H}}{3H^2}\right). \tag{4}$$

Here $H \equiv H(a)$ is the usual Hubble function of the background model. It is convenient now to define a dimensionless parameter Ω_{rc}, which once specified will determine any given nDGP model. Thus, we define

$$\Omega_{rc} \equiv \frac{1}{(2r_cH_0)^2}, \tag{5}$$

with H_0 denoting the present-day value of the Hubble parameter, and the above quantities are expressed assuming $c = 1$. In the phenomenological formulation presented above, the nDGP model admits at large scales a constant enhancement to the Newtonian gravity, which can be evaluated in terms of an effective Newton constant,

$$G_{\mathrm{eff}} = G\{1 + 1/[3\mathcal{B}(a)]\}. \tag{6}$$

This, therefore, leads to a constant enhancement in the linear-theory growth rate of structure f, by a factor $\Delta f = G_{\mathrm{eff}}/G$. On the smaller nonlinear scales, the enhancement of gravity is effectively suppressed by the means of the Vainshtein screening [61,68]. We will study two variants of the nDGP model, specified by $r_cH_0 = 5$ ($\Omega_{rc} = 0.01$) and $r_cH_0 = 1$ ($\Omega_{rc} = 0.25$), which we dub N5 and N1, respectively.

B. $f(R)$ gravity

The $f(R)$ gravity model is an extension of GR that has been extensively studied in the literature in the past several years (see, e.g., [69] for a detailed review). Some previous works have explored this model in different and alternative contexts, such as the internal properties of cosmic structures and their mass-to-light ratio [see, e.g., [70,71]], signatures of $f(R)$ gravity from thermodynamic equilibrium of the clustering of galaxies [72], as well as phenomenological scenarios than the chameleon, symmetron, and $f(R)$ gravity models that scale the local properties of astrophysical systems [73]. The theory is obtained by substituting the Ricci scalar R in the Einstein-Hilbert action with an algebraic function $f(R)$. Here the accelerated expansion of the Universe is produced by this extra term replacing Λ in the action integral, without the need for any form of dark energy. The resulting modified theory of gravity is characterized by highly nonlinear equations of motion for the scalar field, and environment-dependent fifth-force screening is obtained via the so-called "chameleon mechanism" [18,74]. The presence and effectiveness of the chameleon effect is very important for the viability of the $f(R)$-class theories. We comment more on this later on.

One particularly interesting and useful formulation is the so-called Hu & Sawicki [59] branch. Here the functional form of $f(R)$ is

$$f(R) = -m^2\frac{c_1(-R/m^2)^n}{c_2(-R/m^2)^n + 1}, \tag{7}$$

where $n > 0$, c_1, and c_2 are dimensionless free model parameters, and m is an extra mass-dimension parameter. Now, the extra degree of freedom can be again expressed in terms of a scalaron field $f_R \equiv \mathrm{d}f(R)/\mathrm{d}R$, which is not massless, unlike in the case of the nDGP. We can relate the model parameters by writing [59]

$$f_R = -n\frac{c_1}{c_2^2}\frac{(-R/m^2)^{n-1}}{[1 + (-R/m^2)^n]^2}, \tag{8}$$

where the mass scale m is defined as $m^2 \equiv H_0^2\Omega_{\mathrm{m}}$. For this $f(R)$ model, the background expansion history becomes consistent with the ΛCDM case by choosing $c_1/c_2 = 6\Omega_\Lambda/\Omega_{\mathrm{M}}$. The scalaron field f_R adds an additional degree of freedom to the model, whose dynamics in the limit of $|f_R| \ll 1$ and $|f/R| \ll 1$ can be expressed in terms of perturbations of the scalar curvature δR and matter overdensity $\delta\rho$:

$$\nabla^2 f_R = \frac{1}{3}(\delta R - 8\pi G\delta\rho). \tag{9}$$

Comparing to the ΛCDM model expansion history, and under the condition $c_2(R/m^2)^n \gg 1$, the scalaron field can be approximated by

$$f_R \approx -n \frac{c_1}{c_2^2} \left(\frac{m^2}{-R} \right)^{n+1}. \tag{10}$$

Consistency experiments on local gravity such as Solar System constraints, as well as weak and strong equivalence principles constraints, have been set in the bound $n > 0.5$ [see, e.g., [74,75]]. In this paper we consider $f(R)$ models with $n = 1$, which are consistent with the aforementioned constraints.

By setting $n = 1$, the model is fully specified by only one free parameter c_2, which in turn can be expressed in terms of the dimensionless scalaron at present epoch f_{R0}, given by

$$f_{R0} \equiv -\frac{1}{c_2} \frac{6\Omega_\Lambda}{\Omega_m} \left(\frac{m}{2R_0} \right)^2. \tag{11}$$

Therefore, a particular choice of f_{R0} fully specifies the Hu-Sawicki $f(R)$ model. In this work we focus on the cases of $f_{R0} = \{-10^{-5}, -10^{-6}\}$, referred to from now on as F5 and F6, respectively.

At the background level, the $f(R)$ theory can produce significant fifth forces at small noncosmological scales. The presence of such forces is, however, tightly constrained by Solar System and strong-field regime observational tests [75–77]. Here, an essential role is played by the already mentioned chameleon mechanism, which effectively suppresses the fifth force in high density regions. This intrinsically nonlinear mechanism traps the scalar field in high curvature regions making it very massive and suppressing deviations from GR dynamics. There are potentially many interesting nonlinear effects related to the chameleon mechanism that can affect stellar and galaxy evolution [see, e.g., [78]]. Here, we focus on cosmological scales and galaxy clustering, and so the simulations we employ implement self-consistently the chameleon mechanisms only for dark matter clustering in the cosmological context.

III. HALO AND GALAXY MOCK CATALOGS

In this work we consider simulated cosmological data originating from ELEPHANT, introduced in [51,52]. This is based on a suite of dark-matter-only N-body simulations of the standard cosmological model ΛCDM and of the two families of modified gravity theories described above, the nDGP and $f(R)$. The ELEPHANT simulations have been run using the ECOSMOG code [79].

The simulations followed the dynamical evolution of 1024^3 particles placed in a box of $1024h^{-1}$ Mpc comoving width. The evolution of DM phase space was traced from the initial redshift $z_{in} = 49$ down to $z = 0$, with the comoving mass resolution of $m_p = 7.798 \times 10^{10}$ $M_\odot h^{-1}$ and comoving force resolution of $\varepsilon = 15h^{-1}$ kpc equivalent of Plummer softening. For each model we consider five independent phase realizations of the initial power

spectrum, which is derived for the ΛCDM model with the WMAP9 collaboration best-fit parameters [80]: $\Omega_m = 0.281$ (total fractional nonrelativistic matter density), $\Omega_b = 0.046$ (fractional baryonic matter density), $\Omega_\nu = 0.0$ (fractional relativistic matter species density), $\Omega_\Lambda = 1 - \Omega_m$ (cosmological constant energy density), $\Omega_k = 0$ (fractional curvature energy density), $h = 0.697$ (Hubble constant in units of 100 km s^{-1} Mpc^{-1}), $n_s = 0.971$ (primordial power spectrum slope), and $\sigma_8 = 0.820$ (linearly extrapolated ΛCDM power spectrum normalization).

In this work we will deal with DM halos and mock galaxies derived from the ELEPHANT simulations, saved at three cosmic epochs, corresponding to redshifts $z = 0, 0.3$, and 0.5. This particular redshift range is very interesting from both observations and theory vantage points. The currently available redshift survey data, such as the BOSS LOWZ [81], attain the highest galaxy number density in this regime. These redshift ranges will be also probed by future richer data from planned or already ongoing surveys like DESI [32], or 4-metre Multi-Object Spectrograph Telescope Cosmology Redshift Survey [82]. Also, from the theoretical point of view, both the $f(R)$ and nDGP models exhibit the biggest deviations from ΛCDM clustering at low and intermediate redshifts, $0.3 \leq z \leq 0.7$ [e.g., [44,50,83–88]].

The DM halos were identified in the simulations using the ROCKSTAR [89,90] halo finder. It is important to note that on top of using the friends-of-friends approach in 6D phase space, the halo finder performed additionally the gravitational unbinding procedure in which unbound particles are removed from a halo in iterative steps. The standard implementation of this procedure assumes Newtonian gravity for computing the potential and particle binding energy. In $f(R)$ and the nDGP, however, we can arrive at a situation where some halos will be fully or partially unscreened, thus the total fifth force should be added to their binding energy budget. ROCKSTAR does not consider this extra binding energy in its calculations. However, ignoring this extra contribution presents a conservative approach to unbinding: if a particle were not bound in modified gravity, then it would be also definitely unbound in ΛCDM. In addition, the fraction of particles, for which neglecting the extra fifth-force potential would be significant, is very small.

It has been shown that for all practical purposes relevant for this study, one can neglect MG effects in the case of $f(R)$ theories and use the standard Newtonian unbinding procedure [52,91,92]. For the nDGP case, the Vainshtein radius is larger than the biggest objects in our simulations for all the redshifts concerned [17,93], which means that most of the halos should be self-screened.

The galaxy mock catalogs were built using a halo occupation distribution (HOD) prescription [94–96]. The HOD model parameters were tuned for each of the gravity models independently to obtain a catalog matching the

target number density and the projected real-space clustering of BOSS-CMASS galaxies [97]. These galaxy mock catalogs have been exploited in different works, such as [51,52,54,98,99]. In our analysis, we only consider central galaxies, which are located at the center of potential of their host halo. For more details please refer to the original catalog release paper [51].

In our analysis, we adapt M_{200c} as our main halo mass definition. This is defined as the DM mass enclosed within a sphere around the halo center, with the radius r_{200c}, at which the spherically averaged density inside drops down to a value 200 times the critical density of the Universe, i.e., $\rho_c \equiv 3H^2/8\pi G$. Thus, whenever we refer to a halo mass, we mean M_{200c}, unless clearly stated otherwise. Following Ref. [53], from all the raw halo catalogs, we keep for further analysis the halos with at least 64 DM particles. This sets our minimal halo mass to $M_{\min} = 5 \times 10^{12} \, M_\odot h^{-1}$. An important notice here is the fact that the ELEPHANT set is a pure N-body run and, as such, treats all baryonic component as additional collisionless mass. The inclusion of highly nonlinear baryonic physics is fundamental for a proper modeling and understanding in full the galaxy formation process. However, the impact of the full baryonic hydrodynamics for the halo and galaxy clustering and their peculiar velocities has been shown to be minimal [see, e.g., [100]]. Thus, for our purposes here, exclusion of any baryonic physics modeling should not affect our results.

A. Halo mass function and selection of halo populations

The number density of tracers, which in the real survey situation are galaxies, for a volume-limited sample can be simply related to the underlying halo mass function (HMF). The HMF quantifies the comoving number density of DM halos as a function of their mass for a given redshift and cosmology. Since we observe galaxies rather than their host halos, a usual approach is to apply a chosen method of galaxy modeling to obtain the final mock galaxy catalog. In this work, in addition to mock galaxies, we also consider halo populations as tracers. This exercise will allow us to study the modified gravity signal as a function of varying tracer number density. In what follows, we use the halo mass function to select our halo samples choosing their number density to reflect some realistic observational values when using data from the current and next generation of galaxy surveys.

In standard cosmology, HMF can be modeled by, to a high-degree universal, halo multiplicity function giving the number of collapsed objects as a function of the mass field variance expressed at a corresponding scale. In modified gravity the fifth force increases the mass field variance compared to ΛCDM, and so we can expect that the HMF in MG will exhibit differences compared to the fiducial case [55,101–106]. In the cumulative form, the number density of halos above a threshold is given by

$$n(> M_{200c}) = \int_{M_{\min}}^{\infty} \frac{dn}{dM_{200c}} dM_{200c}. \quad (12)$$

Here, as a threshold, we choose a halo mass. The object under the above integral is the differential mass function $dn(M,z)/dM$, which encodes the number of halos per mass interval.

Figure 1 shows the cumulative halo mass function (cHMF) measured from the ELEPHANT simulations and the lower panel shows the relative difference between the MG and GR models at redshift $z = 0.3$. We compare our results from the ELEPHANT simulations to theoretical HMF predictions from [107] (hereafter T08) for both MG models studied. The T08 HMF was calibrated using a spherical overdensity algorithm to identify DM halos in ΛCDM numerical simulations, thus it is consistent with the approach used in ROCKSTAR to identify halos [90]. The T08 HMFs for MG models are not drawn in Fig. 1 since they have the same behavior as that of GR but shifted, following the data points of each model. As shown by the trend of the T08 HMF in Fig. 1, $f(R)$ and the nDGP predict more halos than the ΛCDM model for masses above $10^{12} \, M_\odot/h$, due to the enhancement of gravity [53,84,103,108–111].

The cHMF is of particular interest since it allows us to select different halo populations from the simulations by defining thresholds in halo mass, i.e., selecting halos with masses above a certain value $M_{\min}$ [for details, see
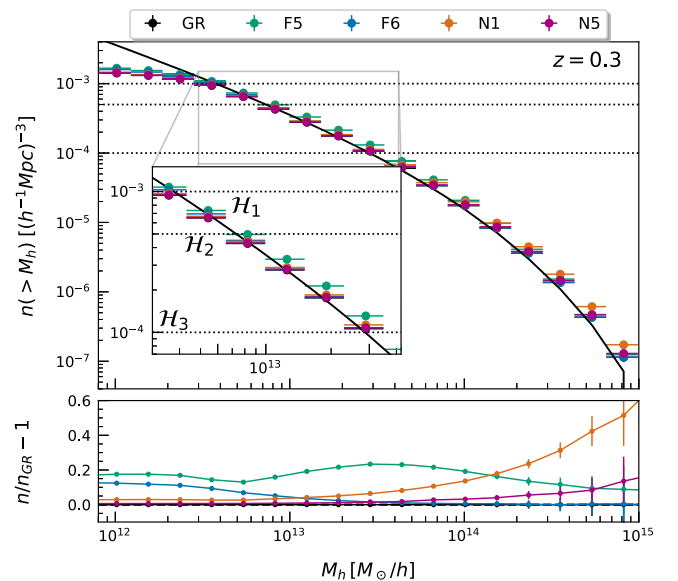

FIG. 1. Cumulative halo mass function for the different ELEPHANT MG models taken at redshift $z = 0.3$. The horizontal dotted lines signal the number densities we use to define our three halo samples. The black solid line represents the theoretical expectation for ΛCDM, given by Tinker *et al.* [107]. The bottom panel shows the relative deviation with respect to the ΛCDM (GR) model with lines connecting the datapoints to guide the eye.

TABLE I. Properties of the halo samples used in this work. In each case, we list the minimum halo mass M_{min} used to obtain the required number density $\bar{n}$ for a given redshift z and gravity model.

z	Halo population	$\bar{n}\ [h^3\ \mathrm{Mpc}^{-3}]$	$M_{\mathrm{min}}[10^{13}h^{-1}\ M_\odot]$				
			GR	F5	F6	N1	N5
0	$\mathcal{H}_1$	10^{-3}	0.319	0.371	0.377	0.326	0.322
	$\mathcal{H}_2$	5×10^{-4}	0.724	0.833	0.805	0.740	0.729
	$\mathcal{H}_3$	10^{-4}	3.42	4.05	3.51	3.56	3.46
0.3	$\mathcal{H}_1$	10^{-3}	0.317	0.387	0.368	0.334	0.321
	$\mathcal{H}_2$	5×10^{-4}	0.705	0.817	0.744	0.728	0.710
	$\mathcal{H}_3$	10^{-4}	3.02	3.55	3.06	3.18	3.06
0.5	$\mathcal{H}_1$	10^{-3}	0.284	0.366	0.323	0.310	0.290
	$\mathcal{H}_2$	5×10^{-4}	0.658	0.770	0.679	0.684	0.663
	$\mathcal{H}_3$	10^{-4}	2.64	3.10	2.65	2.80	2.67

e.g., [53]]. For that we set a fixed number density $\bar{n}(\mathcal{H})$ for each of our halo samples and define M_{min} in each gravity model separately in such a way as to match these number densities. We define three halo populations $\mathcal{H}_1$, $\mathcal{H}_2$, and $\mathcal{H}_3$ with corresponding number densities $\bar{n} = 10^{-4}$, 5×10^{-4}, and $10^{-3}h^3\ \mathrm{Mpc}^{-3}$, respectively.

The galaxy sample, hereafter denoted as $\mathcal{G}$, corresponds to central galaxies inside DM halos, whose distribution can be approximated by a steplike function parameterized in terms of the properties of their host halos. A more detailed description of the HOD modeling can be found in Refs. [51,96]. Our galaxy sample has a number density defined by $\bar{n} = 3.5 \times 10^{-4}h^3\ \mathrm{Mpc}^{-3}$, which is close to that of the $\mathcal{H}_2$ halo sample.

The above number densities have been chosen to be representative of the samples used for cosmological analyses of galaxy surveys such as the SDSS [112], BOSS [5] and eBOSS [113]. We also take into account the resolution limits of the simulations to make sure that the shot noise would not dominate our results. Table I shows the values of the minimum halo mass M_{min} for each gravity model used to obtain the required number density for a given redshift.

IV. CLUSTERING MEASUREMENTS

We characterize the spatial distribution of cosmic tracers in the ELEPHANT simulations (DM particles, halos, and galaxies), in both real and redshift space, with the 2PCF. We use the publicly available code Correlation Utilities and Two-point Estimation [114] to compute the 2D 2PCF with the Landy-Szalay [115] estimator in the comoving range $1 < s\ [h^{-1}\ \mathrm{Mpc}] < 80$ for 20 linearly spaced bins with constant separation $\Delta s = 4h^{-1}\ \mathrm{Mpc}$, in order to compare with previous measurements performed at similar scales [53,54].

In the nonlinear regime, the clustering is well characterized by a much larger variance of the density fluctuations with respect to the one at large scales. In this regime the distortions due to peculiar velocities of the matter tracers

may even exceed the Hubble flow producing a smearing effect known as the "Fingers of God" (FOG) [29]. To model the redshift-space distortions, we construct mock catalogs from the simulations using the distant-observer approximation. The positions in real space **r** are converted into redshift space **s** after adding the contribution due to the peculiar velocities of the tracers along the line of sight (LOS). In order to reduce the impact of cosmic variance in the redshift-space distortions measurements, we average over three different LOSs ($\hat{\mathbf{x}}$, $\hat{\mathbf{y}}$, $\hat{\mathbf{z}}$), then, the errors on the 2PCF measurements are estimated by the standard deviation over fifteen measurements, obtained from the five realizations mentioned in Sec. III. All the models studied here exhibit the same ΛCDM background expansion history, therefore, all redshift-distance relations are the same among them. Figure 2 shows a comparison of the spatial distribution of tracers in real and redshift space for both catalogs of halos and galaxies in a $100h^{-1}\ \mathrm{Mpc}$ thick slice.

The information about clustering anisotropies can be analyzed by computing multipole moments [30,116] and clustering wedges [117,118] from the full 2D 2PCF. In particular, we characterize the clustering either with the first two nonvanishing multipole moments, i.e., the monopole and the quadrupole, or with two clustering wedges of the 2PCF. Considering the expansion only up to the hexadecapole, we can express the 2D 2PCF as follows [116]:

$$\xi(s,\mu) = \xi_0(s)L_0(\mu) + \xi_2(s)L_2(\mu) + \xi_4(s)L_4(\mu), \quad (13)$$

with $L_l(\mu)$ being the Legendre polynomials of degree l and the coefficient of the expansion corresponding to the lth multipole moment of the 2PCF:

$$\xi_l(s) \equiv \frac{2l+1}{2} \int_{-1}^{+1} \mathrm{d}\mu\, \xi(s,\mu)L_l(\mu). \quad (14)$$

Here $\mu \equiv \cos(|\vec{s}|/s_\parallel)$ is the cosine of the angle between the separation vector of the tracer pair and the LOS direction.
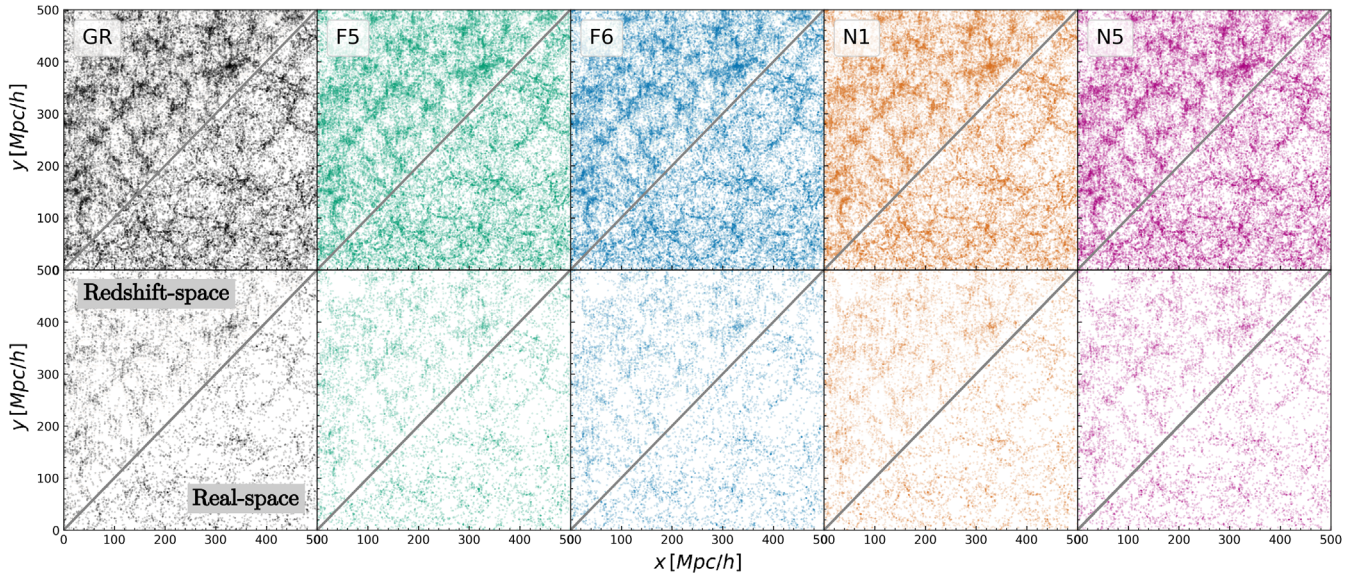
FIG. 2. Spatial distribution of DM halos (top panels) and HOD galaxies (bottom panels) in a $100h^{-1}$ Mpc thick slice from the ELEPHANT simulations at redshift $z = 0$. The data represented above (below) the diagonal of each box correspond to the redshift (real) space distribution. DM halos are plotted in the mass range $[10^{12}, 2 \times 10^{15}] \, M_\odot/h$.

An alternative and complementary measure to the multipole moments are the clustering wedges [117], which correspond to the angle-averaged $\xi(s_\perp, s_\parallel)$ over wide bins of μ such that

$$\xi_w(s) \equiv \frac{1}{\Delta\mu} \int_{\mu_1}^{\mu_2} \xi(s, \mu) \mathrm{d}\mu, \qquad (15)$$

where $\Delta\mu = \mu_2 - \mu_1$ is the wedge width. We consider two clustering wedges, that is the "transverse" wedge $\xi_\perp(s) \equiv \xi_{1/2}(\mu_{\min} = 0, s)$ and the "radial" (or LOS) wedge $\xi_\parallel(s) \equiv \xi_{1/2}(\mu_{\min} = 0.5, s)$, computed in the ranges $0 \leq \mu < 0.5$ and $0.5 \leq \mu \leq 1$, respectively. In this work, both multipole moments and wedges are measured via numerical integration of the full 2D 2PCF in the plane-parallel approximation according to Eqs. (14) and (15), respectively.

The deviations in clustering between GR and MG models can be quantified through the linear distortion parameter $\beta \equiv f(z)/b(z) \approx \Omega_m^\gamma(z)/b(z)$, where γ is the so-called growth index, $f(z)$ is the linear growth rate, and $b(z)$ is the linear bias parameter, which relates the cosmic tracers with the DM density field [33,47,119–125]. The linear distortion parameter is expressed in terms of the amplitude of the distortions of the clustering. To obtain β, one can use as an estimator the ratio between the redshift space and real-space monopole, denoted as $R(s)$, as well as the ratio between the redshift-space quadrupole and the monopole, denoted as $Q(s)$ [55,126–129]. We note, however, that these estimators only perform well in the linear regime. These quantities can be written as follows [21]:

$$R(s) = \frac{\xi_0(s)}{\xi_0(r)} = 1 + \frac{2\beta}{3} + \frac{\beta^2}{5}, \qquad (16)$$

$$Q(s) = \frac{\xi_2(s)}{\xi_0(s) - \frac{3}{s^3}\int_0^s ds' \xi_0(s')s'^2} = \frac{\frac{4}{3}\beta + \frac{4}{7}\beta^2}{1 + \frac{2\beta}{3} + \frac{\beta^2}{5}}, \qquad (17)$$

where ξ_0 and ξ_2 are the monopole and quadrupole of the 2PCF, respectively.

V. RESULTS

We now present the results of our analysis, accompanied by a detailed discussion. A busy reader can skip to the conclusions in Sec. VII, where we cover all the important findings supplemented by the final discussion. The clustering analysis of the different halo populations and the galaxy sample has been performed at three different cosmic times as mentioned in Sec. IV. However, below we will focus on $z = 0.3$, which is compatible with the BOSS LOWZ galaxy sample ($z \lesssim 0.4$), and we will only refer to the other redshifts where relevant.

A. Clustering in real space

The distribution of matter and halos in the real space is characterized by statistical isotropy among all spatial directions, in a sense of an ensemble average. This means that all the higher multipole moments of the 2PCF with $l > 0$ vanish. Thus, the matter clustering is encoded in the monopole moment of the 2PCF $\xi_0(r)$. Figure 3 shows the real-space 2PCF of ELEPHANT at redshift $z = 0.3$ for the
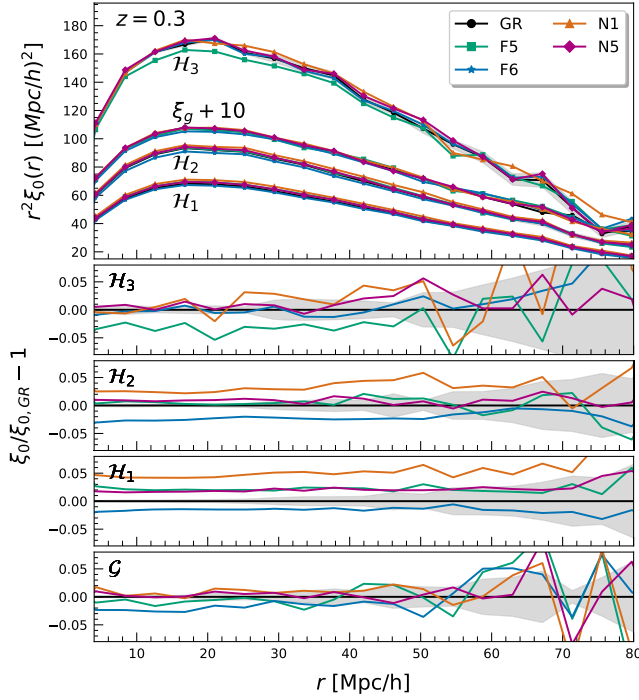
FIG. 3. Real-space monopole of the 2PCF of halos and galaxies at redshift $z = 0.3$ for tracers indicated by the labels. The lower panels show the relative difference of MG models with respect to ΛCDM. The grey-shaded areas indicate the propagated measurement errors for ΛCDM over fifteen measurements.

three different halo populations and the galaxy sample for the considered gravity models. The galaxy correlation function closely follows the result for the $\mathcal{H}_2$ population, so it was shifted upwards by 10 units to facilitate a better visualization. The lower panels show the relative difference of MG models with respect to ΛCDM. The results for other redshifts are qualitatively similar, and we do not show them here in the interest of space. Quantitatively, by comparing the 2PCFs, we observe that, for a given MG model, the amplitude of the clustering increases with cosmic time, as expected, being higher for lower the redshifts. The clustering amplitude depends strongly on the mass cut of the tracer distribution, and as a consequence, denser samples are much more sensitive to clustering, the extreme case being the one given by the sample $\mathcal{H}_1$. This variation in the clustering is present in all the MG models investigated, being also an expected feature since the models share the background history and, therefore, reproduce a hierarchical structure formation starting from the same initial conditions [38,130,131].

For the most sparse sample of $\mathcal{H}_3$, all MG models except F5 exhibit the shape and amplitude consistent with that of the GR case. For the higher number density samples, differences among models start to become more apparent and significant. For $\mathcal{H}_2$, the N1-case experiences enhanced clustering, and this signal appears to be significant on nearly all scales up to $70h^{-1}$ Mpc. This deviation attains a

maximum at $r \simeq 50h^{-1}$ Mpc, where it amounts to a 5% increase of the ξ_0 amplitude. In contrast, the F6 model is characterized by a lower correlation strength over the separation range of $5 \leq r[h^{-1}$ Mpc$] \leq 50$. The N5 and F5 models for this sample exhibit deviations from GR that are typically smaller than 1%. Moving to our highest density halo sample $\mathcal{H}_1$, we observe very similar trends as for the other halo populations, but now the N1 and F6 models also foster small, but significant, deviations from the GR case. The increased statistical significance of the departures that we can appreciate for this sample show a clear advantage of the increased number density, providing better sampling of the density field. For N5 and F5, the increase of the correlation amplitude over ΛCDM is small, at the 2% level, but appears to be significant up to pair separations of $r \simeq 45h^{-1}$ Mpc.

Last but not least, for the galaxy sample $\mathcal{G}$, the general impression is that the MG-induced deviations are very much suppressed for all the models. This is not surprising, accounting for the fact that the HOD mock galaxy catalogs were constructed to have the same (consistent with observations) amplitude of the projected correlation function $w_p(r_p)$, up to a maximum 1% variation [51,52]. Despite this, for F5 and F6 at $r \leq 30h^{-1}$ Mpc, we can still observe some remaining minute differences below 2%. This is related to the fact that significant differences prevail in the real-space 3D correlation function, suggesting that the chameleon mechanism (operating efficiently on small nonlinear scales) leaves a lasting imprint on the $f(R)$ galaxy clustering on those scales (see also [83]).

The scalaron fifth force affects more significantly the growth of structures in the F5 model than in F6, that itself mostly agrees with the ΛCDM clustering signal, especially for low number density samples, such as $\mathcal{H}_3$. This effect is neither appreciable for higher number densities as in $\mathcal{H}_1$ nor in the galaxy sample as shown in Fig. 3. This behavior is well understood considering the weak modifications introduced to GR by the scalar field in the F6 model, therefore, only deviations within a few percent are expected. The above results are in agreement with the analyses performed with different simulations that also include the same MG models [53,54,110,111].

B. Linear halo and galaxy bias

The simplest way of expressing the relation between biased tracers (halos and galaxies) and the underlying smooth DM density field is given by the linear bias parameter b. This is defined as $b \equiv \delta_x/\delta$, where δ is the DM density contrast, δ_x is the density contrast of the tracers, and the subscript $x = \{g, h\}$ denotes galaxies or halos, respectively. The linear bias can be estimated from the ratio of the real-space autocorrelation functions of the tracer and DM field as follows:
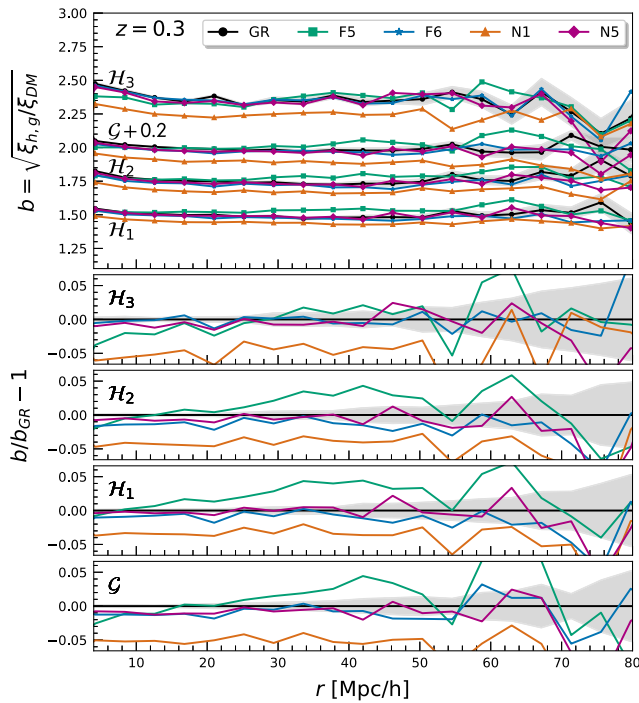
FIG. 4. Effective linear halo and galaxy bias as a function of the comoving scale at redshift $z = 0.3$ for tracers indicated by the labels. The lower panels show the relative difference of MG models with respect to the ΛCDM model. The gray-shaded areas indicate the propagated measurement errors for ΛCDM over fifteen measurements.

$$b(M, r, z) = \sqrt{\frac{\xi_x(M, r, z)}{\xi_{\mathrm{DM}}(r, z)}}. \qquad (18)$$

From the above we can expect that the relation between the density field of tracers and the smooth background can be generalized to a more complicated form, usually involving some scale dependency. In the following analysis we will not attempt to model any such beyond-linear bias dependence. We are motivated by the fact that the scale dependence of the bias is weak on the large enough scales (i.e., $\geq 30h^{-1}$ Mpc) [27,132–135].

In Fig. 4 we show the measured halo (galaxy) bias as a function of the comoving scale. In each case the shaded area corresponds to the mean value and 1σ scatter for the ΛCDM model. The bottom panels illustrate the relative difference for each sample and each model with respect to the ΛCDM case. The data shown here support our stipulation of very weak scale dependence of the linear bias, which is confirmed for all our samples and models. The trend shown in Fig. 4 indicates that the linear bias decreases monotonically with the growing number density for all the models. Moreover, the deviation with respect to the ΛCDM model is more significant in high density halo populations, such as $\mathcal{H}_1$ than in the low density ones, for all models except N1, which exhibits a prominent deviation in

the $\mathcal{H}_3$ case. At the same time, the relative deviation in the linear bias is almost constant in all the MG models for scales up to $60h^{-1}$ Mpc.

Looking more closely at model-specific cases, it is clear that for both F6 and N5 the differences from the ΛCDM are minute and hence insignificant given our sample variance. This is expected, considering that these two variants should exhibit the weakest deviations from the standard structure formation scenario. Consequently, the stronger variants of $f(R)$ and the nDGP models are characterized by much clearer and more significant departures from the GR case. This is especially highlighted for the bias of the N1 model, which takes systematically lower values then GR for all the probed scales. These differences appear relatively flat with distance and amount steadily to about $\sim -5\%$ for all the samples, including galaxies. The F5 variant appears here as the most variable and interesting one: its linear bias difference with respect to the fiducial case exhibits clearly both scale and sample dependence. For the low-density sample $\mathcal{H}_3$, the difference is small and, except for the smallest separations, nonsignificant. The situation is quite the opposite for the high density samples, where we observe a peak of $\sim +4\%$ around $r \sim 40h^{-1}$ Mpc. This relative difference appears to be strongly suppressed at $r \sim 55h^{-1}$ Mpc (where for $\mathcal{H}_3$ it even takes a minus sign), to again grow beyond $+5\%$ at $r \sim 60h^{-1}$ Mpc. However, we believe that the feature at $60h^{-1}$ Mpc is rather artificial than due to any genuine physical effects. This is related to the fact that the linear bias is a ratio of two estimators that, due to the limited-volume effects, become more and more noisy with the growing scale, while the relative difference with respect to the ΛCDM case is itself based on a ratio. In addition, we know that all the involved numbers are small. These all affect significantly the ratio in question, making it very noisy for $r \gtrsim 50h^{-1}$ Mpc.

From the above analysis, illustrated in Fig. 4, a very important picture emerges. The bias of galaxy and halo fields in MG can be significantly different from the GR case, and the effect in general can take both the positive and negative sign. Moreover, the differences depend on the sample density (hence implicitly on the tracer mass). This has been already pointed out by some earlier work [136,137]. The sample density could potentially introduce a degeneracy of the MG effect with the growth rate, therefore, the latter parameter could be much closer to the GR expectation than it really is.

Following Eq. (18), we estimate the effective linear bias b based on an χ^2 fit to the square root of the ratio of the tracer 2PCF and the DM 2PCF over the comoving range $40 < r[h^{-1}$ Mpc$] < 80$ for each model, sample, and redshift from ELEPHANT simulations. Table II shows a summary of the measured galaxy and halo bias for all the considered gravity models at three different redshifts $z = 0$, 0.3, and 0.5. Figure 5 displays the evolution of the effective bias as a function of redshift with error bars that represent

TABLE II.   The effective linear galaxy and halo bias $b(z)$ estimated from Eq. (18) for all gravity models at three different redshifts $z = 0$, 0.3, and 0.5.

z	Sample	GR	F5	F6	N1	N5
0	$\mathcal{G}$	1.59 ± 0.04	1.61 ± 0.05	1.61 ± 0.05	1.50 ± 0.04	1.55 ± 0.04
	$\mathcal{H}_1$	1.30 ± 0.03	1.33 ± 0.04	1.30 ± 0.04	1.27 ± 0.03	1.29 ± 0.03
	$\mathcal{H}_2$	1.50 ± 0.04	1.52 ± 0.05	1.50 ± 0.05	1.45 ± 0.04	1.48 ± 0.04
	$\mathcal{H}_3$	2.00 ± 0.07	2.02 ± 0.08	2.02 ± 0.08	1.91 ± 0.06	1.94 ± 0.07
0.3	$\mathcal{G}$	1.80 ± 0.05	1.83 ± 0.05	1.77 ± 0.05	1.67 ± 0.05	1.76 ± 0.05
	$\mathcal{H}_1$	1.49 ± 0.04	1.54 ± 0.04	1.47 ± 0.03	1.44 ± 0.04	1.49 ± 0.04
	$\mathcal{H}_2$	1.75 ± 0.05	1.80 ± 0.05	1.72 ± 0.04	1.68 ± 0.05	1.74 ± 0.05
	$\mathcal{H}_3$	2.35 ± 0.08	2.35 ± 0.08	2.34 ± 0.08	2.23 ± 0.08	2.34 ± 0.08
0.5	$\mathcal{G}$	1.94 ± 0.06	1.95 ± 0.07	1.95 ± 0.06	1.85 ± 0.05	1.88 ± 0.07
	$\mathcal{H}_1$	1.61 ± 0.05	1.63 ± 0.05	1.60 ± 0.04	1.56 ± 0.04	1.58 ± 0.05
	$\mathcal{H}_2$	1.92 ± 0.06	1.93 ± 0.06	1.91 ± 0.05	1.84 ± 0.05	1.86 ± 0.06
	$\mathcal{H}_3$	2.58 ± 0.11	2.52 ± 0.12	2.59 ± 0.10	2.47 ± 0.10	2.51 ± 0.10

the 1σ statistical error. The solid lines correspond to the theoretical prediction computed using the Tinker *et al.* [138] formula and by averaging the linear bias $b(M, z)$ of the selected sample as follows:

$$ b_{\mathrm{eff}}(z) = \frac{\int_{M_{\min}}^{M_{\max}} n(M, z) b(M, z) dM}{\int_{M_{\min}}^{M_{\max}} n(M, z) dM}, \qquad (19) $$

where the mass limits $[M_{\min}, M_{\max}]$ have been defined in Sec. III, while $n(M, z)$ and $b(M, z)$ are estimated using the Tinker *et al.* [107] mass function and the Tinker *et al.* [138] bias model, respectively. The trend in the bias confirms that

the nDGP models differ the most from the standard model predictions both for halo and galaxy samples. Instead, the $f(R)$ models are in good agreement with ΛCDM, and they deviate less at low redshifts than the nDGP ones.

C. Clustering in redshift space

Figure 6 shows the full 2D 2PCF computed at a redshift $z = 0.3$ as a function of the transverse $s_\perp$ and parallel $s_\parallel$ separations with respect to the LOS. The black line marks the result for the ΛCDM model from ELEPHANT simulations, while each MG model is depicted by a different color. Each quadrant shows the 2PCF signal for a different tracer
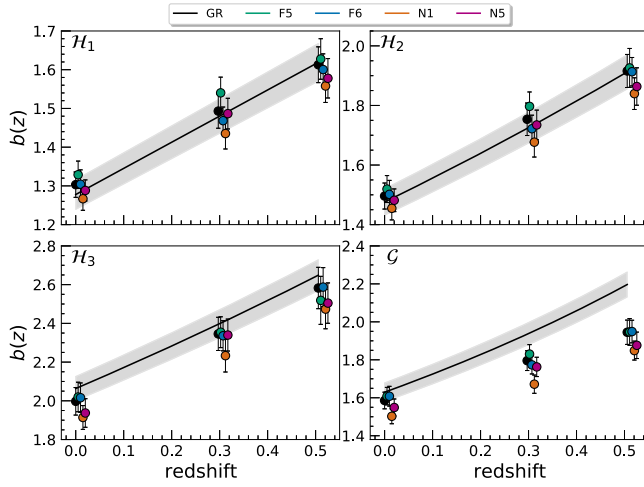

FIG. 5.   Effective halo (galaxy) bias averaged in the range $40 < r[h^{-1} \mathrm{Mpc}] < 80$ as a function of redshift for the models considered in this work. The plot shows the bias at redshifts $z = 0, 0.3$, and 0.5, however, for a better visualization the redshift of the MG models has been shifted from the mean value. Solid line shows the theoretical ΛCDM prediction computed according to the Tinker *et al.* [138] formula. The error bars represent the propagated statistical noise and the gray-shaded areas show a 3% error.
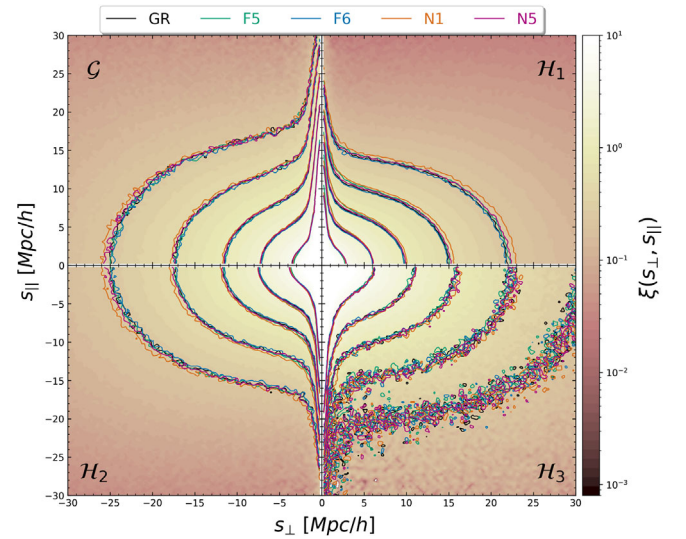

FIG. 6.   Isocorrelation contours of $\xi(s_\perp, s_\parallel)$ at the reference redshift $z = 0.3$ for the models indicated in the legend, shown for correlation amplitude levels $\xi(s_\perp, s_\parallel) = \{0.25, 0.5, 1, 2, 5\}$. Each quadrant corresponds to a different tracer sample (halos and galaxies) as labeled. The color bar to the right and the background color of the panels indicate the amplitude of $\xi(s_\perp, s_\parallel)$ for ΛCDM as the reference model.

sample (galaxies and halo populations) as labeled. The isocorrelation contours of $\xi(s_\perp, s_\parallel)$ are measured in the amplitude range [0.25, 5]. The resulting contours of galaxy samples for the different gravity models are very close to each other, with the slight exception of the N1 model. This is not surprising, as the correlation in redshift space is determined, to the first order, by the amplitude of real-space correlations [30]. The latter are by design set to be equal among all the mock catalogs. A more careful statistical inspection of the moments of 2D 2PCF would be needed to highlight MG effects for our galaxy samples.

Halo clustering, likewise to mock galaxies, shows slight differences for all MG models. These are best visible for the populations with medium $\mathcal{H}_2$ and high number densities like $\mathcal{H}_1$. The clustering signals from the $\mathcal{H}_3$ populations are noise dominated at all scales, as expected, and therefore, there is no visible distinction between the MG models and GR. In the most abundant halo population $\mathcal{H}_1$, there is a clear difference between the GR case and the N1 model, which displays an excess in the clustering. On the contrary, the $f(R)$ gravity variants exhibit a slight suppression in the clustering signal at all scales. This behavior can be also seen, although to a lesser extent, at small comoving scales, $\sim 4h^{-1}$ Mpc, despite a very similar amplitude in the FOG for all MG models. However, a conclusive analysis on these scales would require high-resolution simulations plus the implementation of additional physical processes, which are relevant at those scales. In the three halo selections for all our MG models, the 2PCF for N1 deviates the most from the GR case. For the other models, the differences, albeit noticeable in the 2PCF isocontours, are much harder to depict. In general, as the halo number density decreases, the differences between MG and GR get smaller. In addition, the selection effects related to the changing number density (which itself is here driven by the minimum mass cut) shows how RSD are affected at all scales. The amplitude of clustering varies more in the transverse direction than in the LOS, indicating that the Kaiser squashing effect is more sensitive to the coherent motion of the tracers than the FOG under the same mass selection.

The complicated pattern and relatively small differences among the models, as seen in the 2D 2PCF, suggest that a more elaborate analysis is needed to robustly quantify MG effects. As previously pointed out in Sec. IV, projecting $\xi(s_\perp, s_\parallel)$ onto one-dimensional statistics (multipole moments or wedges) increases the clustering signal and disentangles the directional dependence on clustering. In Fig. 7 we show the redshift-space multipole moments $\xi_l(s)$ (upper group of plots) and clustering wedges $\xi_w(s)$ (lower group of plots), measured for our halo and galaxy samples at $z = 0.3$ for the different MG models, as labeled. In each case the lower subpanels show the relative differences with respect to the ΛCDM measurements.

As far as the monopole $\xi_0(s)$ is concerned, we firstly observe that it decreases as the number density increases,

mainly due to the difference in the bias of each sample, as expected. The clustering signal of the medium number density halo sample $\mathcal{H}_2$, follows closely the monopole of the galaxy sample, which in Fig. 7 has been shifted by 10 units for visual convenience. For all our samples, both the nDGP models exhibit a rise in the correlation amplitude seen at all probed scales. There is also a general trend of the braneworld gravity enhanced clustering signal that is dropping with decreasing sample number density. In contrast, the situation for the $f(R)$-gravity family is quite different. Here, the effect on the monopole amplitude goes generally in the opposite direction, and the clustering at fixed number density seems to be slightly suppressed. The exception from this is F5 in the richest halo sample of $\mathcal{H}_1$. Another observation regarding the correlation function monopole is that the differences in this statistic between the MG models and the fiducial ΛCDM case generally do not correlate with the magnitude of deviations (e.g., level of the fifth force) of the particular MG variants. While for the nDGP, the monopole signal for N1 is always larger than for N5, in the chameleon $f(R)$, for some samples (i.e., $\mathcal{G}$ and $\mathcal{H}_2$), it is the F6 variant that departs more prominently, while for others (i.e., $\mathcal{H}_1$ and $\mathcal{H}_3$) the F5 deviates more. Finally, while for the braneworld models the excess clustering signal is relatively flat with the pair-separation scale, in $f(R)$ the differences are scale dependent and suppressed for $s \geq 60h^{-1}$ Mpc.

Overall, the behavior of $\xi_0(s)$ that we described above supports the known picture in which the $f(R)$ gravity models are characterized by a very high degree of nonlinearity, even at larger scales. This is a clear virtue of the chameleon screening mechanism: its effectiveness is a function of the local environment, so it operates in a more complicated manner than the Vainshtein screening of the nDGP. The nonlinear and nonmonotonic behavior of the $f(R)$ clustering signal, as compared to the nDGP, could be, in principle, exploited for differentiating these two classes of screening mechanisms in the data.

The quadrupole moment of the 2PCF $\xi_2(s)$, illustrated in the upper-right panel of Fig. 7, encodes the degree of anisotropy generated by RSD. For all our samples, there is only one model, N1, which fosters clear deviations from the fiducial GR case, while the effect for N5 is only marginally significant. Taking into account the scatter, both $f(R)$ models exhibit a signal that is statistically consistent with the GR case. The noisy behavior that we see at $s \leq 20h^{-1}$ Mpc, rather than a real physical feature, is likely a manifestation of sampling noise to which the quadrupole moment is more susceptible. The noise at those small pair separations is additionally increased, owing to the fact that we consider only halos and central galaxies, and due to the halo-exclusion effect, the pair number counts are suppressed at small scales. There could be, in principle, a real physical MG signal encoded at those small scales, but the properties of our simulations and catalogs are not designed to grant such analysis at this time.
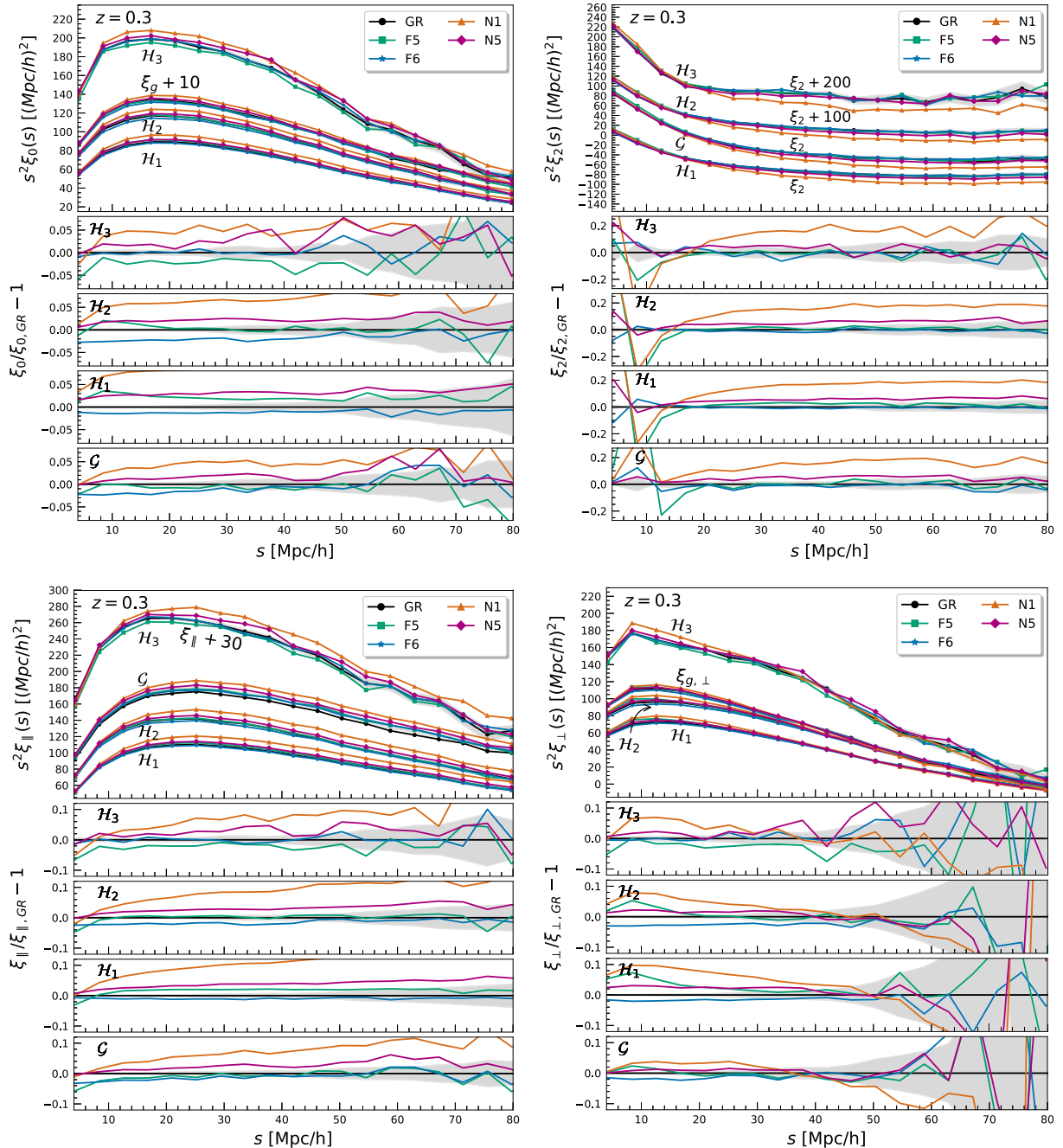
FIG. 7.   Redshift-space multipole moments of the 2PCF ξ_0 and ξ_2 (upper panels) and clustering wedges $\xi_\parallel$ and $\xi_\perp$ (lower panels) for the different gravity models and tracer samples used in this work as indicated by the labels. The lower subpanels in each row show the difference of MG models with respect to the ΛCDM measurements. The gray-shaded areas correspond to the standard deviation for ΛCDM over fifteen measurements obtained from five different realizations.

The analysis of the clustering wedges (see Fig. 7, lower panels) paints a picture complementary to the one offered by the multipoles. It is worth noting that the clustering anisotropies, as measured in each of the two angular wedges, disclose stronger MG signals than it was in the case for the multipole moments. Here, the relative deviation from GR of the LOS wedge $\xi_\parallel(s)$, for the nDGP models,

reaches 10% (5%) for N1 (N5). This is roughly a factor of two more than we saw in the monopole analysis. What is even more important is that the increased relative difference is not affected by the statistical error, which remains at a level similar to that of the monopole measurements. Our results agree here with the earlier work of Barreira *et al.* [50], who studied clustering wedges for similar variants of

the nDGP models. This opens up an exciting avenue of using the clustering wedge statistics to hunt for the MG signal in galaxy clustering.

The changes in the clustering are also manifested in the transverse wedge $\xi_\perp(s)$, which gives valuable information from an observational point of view, considering the degeneracy between RSD and other observational phenomena such as the Alcock-Paczyński effect [139]. The difference between GR and MG seen in the amplitude of the transverse wedge reveals a few interesting facts. First, we notice that for the perpendicular projection the deviations in clustering of galaxy samples for all MG models are much smaller than it was in the case for the LOS direction. This is driven by the fact that the same projected clustering $w_p(r_p)$ was imposed in the construction of mock galaxy catalogs. In contrast, different halo populations reveal somewhat larger deviations from the GR case. Second, the MG effect seen in $\xi_\perp(s)$ seems to be contained only to small scales $s \leq 40h^{-1}$ Mpc. Here, the maximal deviations are attained at the highly nonlinear separations of $10h^{-1}$ Mpc. Furthermore, the transverse wedge of the N1 model deviates from GR by about 10% at small scales $s < 20h^{-1}$ Mpc, although this behavior is also displayed by the multipole moments. In this case the angular clustering signal is well characterized by a monotonically decreasing function, being almost independent of the number density of the halo sample.

D. Linear distortion parameter β

All the effects revealed by our analysis of the multipoles and wedges should lead to measurable differences in the linear-theory growth-rate parameter f, as estimated by various combinations of the clustering statistics. Since we are measuring clustering of biased traces (i.e., halos and galaxies), we cannot directly measure the growth rate. Instead, we can estimate the linear distortion parameter β by fitting the combinations of the measured multipole moments $Q(s)$ to the function given by Eq. (17). Following earlier related studies [e.g., [51,54]], we only keep the results derived from $Q(s)$ since it already contains the information from $R(s)$ in its denominator. The dependence on the quadrupole suggests that the $Q(s)$ estimator could be more prone to noise than the $R(s)$ ratio alone. However, it is more advantageous to use the former as it does not depend on the shape of $\xi(r)$ [116,140]. Thus, when comparing with observational data, no assumptions on the DM clustering signal in the real space are required. To estimate $\beta(z)$ from the quadrupole ratio $Q(s)$, we perform an χ^2 minimization for each of the models, samples, and redshifts separately.

Figure 8 shows our β measurements as a function of redshift for all our samples and models. The 1σ error bars on β have been estimated via direct propagation of the uncertainties of $Q(s)$ since it is a one-parameter model. The solid line represents the linear theory prediction for GR computed using the bias prescription of Ref. [138] and growth rate of the fiducial cosmology, while the shaded
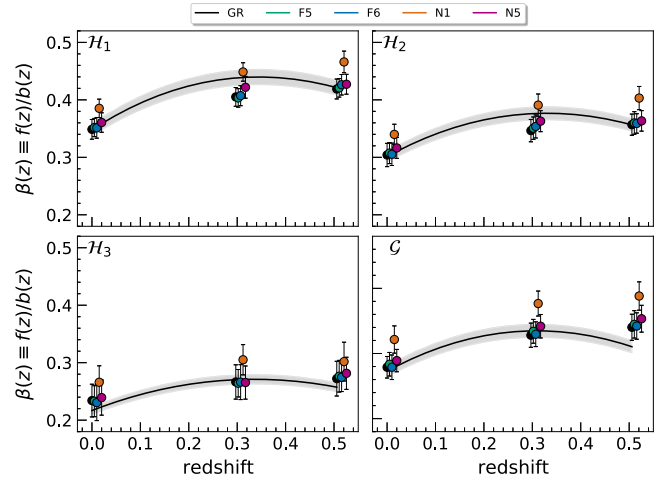

FIG. 8. Linear distortion parameter $\beta(z)$ of halos (galaxies) from ELEPHANT simulations as a function of redshift for the models considered in this work. For better visualization the datapoints for the MG models have been shifted horizontally from the mean values $z = 0, 0.3$, and 0.5. Solid lines show the theoretical ΛCDM prediction computed according to the Tinker *et al.* [138] bias prescription and growth rate of fiducial cosmology. The error bars represent the propagated statistical noise and the gray-shaded areas show a 3% error on β for comparison.

region corresponds to a 3% deviation from it. This percentage is for reference, and it is well below the current errors on β obtained from observations such as the 6-degree Field Galaxy Survey (6dFGS). Adams *et al.* [141] have recently reported statistical uncertainty on β of about 15% and systematic one of $\sim$17% from this survey. Table III displays the best-fit values of β for all the samples and models investigated. As it can be appreciated, our constraint for the linear distortion parameter at $z = 0$ is in good agreement with the value by [141], $\beta = 0.289^{+0.044}_{-0.043}(\text{stat}) \pm 0.049(\text{sys})$, which was based on joint measurements of RSD and peculiar velocities from the 6dFGS.

In Fig. 9 we additionally show the β parameter values as a function of the number density of our samples. The results are plotted for three different redshift snapshots $z = 0, 0.3$, and 0.5, as indicated by the labels. The solid black line represents the linear-theory prediction for β at the given number densities of the samples in the GR scenario. The points that correspond to particular number densities are connected using straight lines for visualization. The shaded region also corresponds to a 3% deviation from the GR prediction, as in Fig. 8. Beside synthesizing our previous findings, Fig. 9 allows us to additionally describe the behavior of β in terms of both the sample density (hence corresponding tracer halo mass) and its redshift. In particular, we note a monotonic increase of β with increasing number density. Although the changes in the predicted slope are not dramatic when comparing the different redshifts, the slight shift of β shows its sensitivity with

TABLE III.   Best-fitting values of the linear distortion parameter $\beta(z)$ of halos and galaxies, obtained using the $Q(s)$ estimator, Eq. (17).

z	Sample	GR	F5	F6	N1	N5
0	$\mathcal{G}$	0.279 ± 0.017	0.283 ± 0.018	0.279 ± 0.019	0.321 ± 0.021	0.289 ± 0.017
	$\mathcal{H}_1$	0.349 ± 0.017	0.352 ± 0.016	0.351 ± 0.018	0.385 ± 0.016	0.361 ± 0.017
	$\mathcal{H}_2$	0.304 ± 0.020	0.307 ± 0.018	0.305 ± 0.019	0.340 ± 0.018	0.316 ± 0.018
	$\mathcal{H}_3$	0.234 ± 0.028	0.233 ± 0.027	0.231 ± 0.031	0.266 ± 0.029	0.239 ± 0.031
0.3	$\mathcal{G}$	0.328 ± 0.019	0.334 ± 0.018	0.330 ± 0.019	0.377 ± 0.019	0.342 ± 0.018
	$\mathcal{H}_1$	0.405 ± 0.016	0.403 ± 0.016	0.407 ± 0.017	0.449 ± 0.016	0.422 ± 0.019
	$\mathcal{H}_2$	0.346 ± 0.019	0.351 ± 0.020	0.354 ± 0.020	0.391 ± 0.019	0.363 ± 0.018
	$\mathcal{H}_3$	0.266 ± 0.030	0.264 ± 0.024	0.266 ± 0.030	0.305 ± 0.026	0.265 ± 0.029
0.5	$\mathcal{G}$	0.340 ± 0.020	0.345 ± 0.021	0.342 ± 0.020	0.388 ± 0.022	0.353 ± 0.021
	$\mathcal{H}_1$	0.419 ± 0.017	0.421 ± 0.016	0.426 ± 0.018	0.466 ± 0.019	0.427 ± 0.017
	$\mathcal{H}_2$	0.357 ± 0.018	0.360 ± 0.020	0.359 ± 0.017	0.403 ± 0.020	0.363 ± 0.018
	$\mathcal{H}_3$	0.272 ± 0.030	0.276 ± 0.028	0.275 ± 0.025	0.302 ± 0.034	0.282 ± 0.028

respect to the sample density and, consequently, the impact of the degeneracy between the halo or galaxy bias and the growth factor.
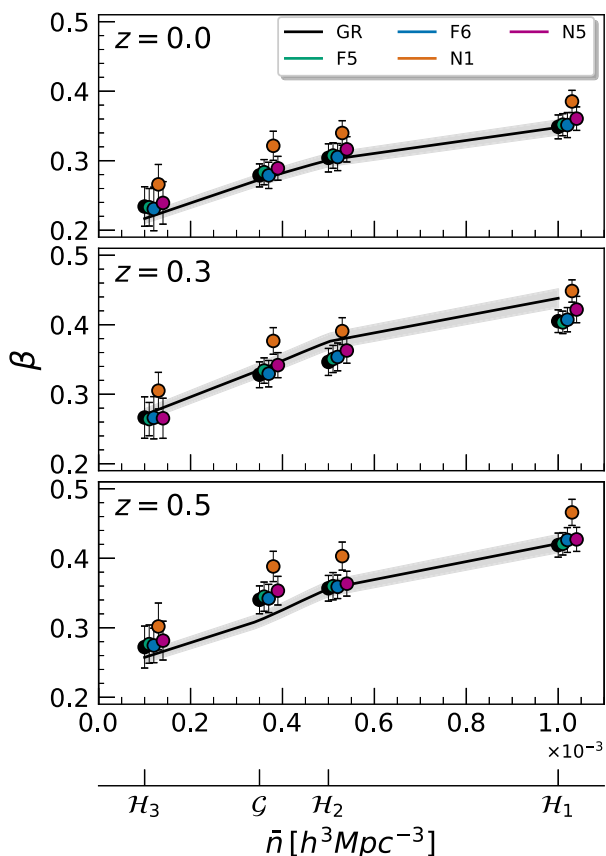

FIG. 9.   Linear distortion parameter $\beta(z)$, as a function of the number density of the tracer samples used in this work (halos and galaxies). Results for three different redshifts $z = 0, 0.3$, and 0.5 are shown as indicated by the labels. The error bars represent the propagated statistical noise and the gray-shaded areas show a 3% error.

The Q estimator offers, in principle, also a possibility to determine the growth rate. To do so, however, one needs to either obtain information on the value of the sample galaxy bias parameter or assume one. In general, it is not always guaranteed that a simple linear theory prediction for the bias will lead to an accurate growth rate estimate from the distortion parameter. In some cases the linear bias relation might not be an adequate description of the data, and therefore, higher order bias approximations may be required to account for the scale dependency [142–145]. In fact, the Kaiser [30] enhancement is sensitive to the physics on nonlinear scales. Some of these effects might not be captured entirely by our relatively low resolution N-body simulations. In particular, when β is determined from the quadrupole to monopole ratio, the systematic errors are significant even at the scales considered. This can be well appreciated by noticing that even our ΛCDM measurements are not in perfect agreement with the linear theory predictions. For this reason, we attempt to recover the true value of the distortion parameter in a bias-independent fashion. As described in the following Sec. VI, we generalize the clustering estimator initially proposed by Arnalte et al. [53], which allows us to analyze the clustering signal with less impact of halo and galaxy bias and, at the same time, increase the signal-to-noise ratio of the correlation function.

VI. RELATIVE CLUSTERING ANALYSIS

The above-discussed estimators of the distortion parameter β, based on the $Q(s)$ and $R(s)$ ratios, depend strongly on the bias, and therefore, the straightforward interpretation of the clustering is limited by the degeneracy between the growth rate and the bias, both encoded in β. Those ratios might also suffer from a theoretical model bias since they ignore the effects of the LOS velocity dispersion [see, e.g., [41]]. To foster analysis of clustering observables that would be less dependent on the bias model, we will now consider an estimator inspired by Arnalte-Mur et al. [53],

TABLE IV. The amplitude of the multipole moments (upper part) and clustering wedges (lower part) of the 2PCF for GR at the reference scale s_{ref} used in the clustering ratios.

| z | Sample | $\xi_0(s_{ref})$ | | $\xi_2(s_{ref})$ | |
		$16h^{-1}$ Mpc	$64h^{-1}$ Mpc	$16h^{-1}$ Mpc	$64h^{-1}$ Mpc
0	$\mathcal{H}_{ref}$	0.314 ± 0.001	0.011 ± 0.001	-0.141 ± 0.001	-0.018 ± 0.001
	$\mathcal{G}_{ref}$	0.449 ± 0.001	0.015 ± 0.001	-0.109 ± 0.002	-0.021 ± 0.001
0.3	$\mathcal{H}_{ref}$	0.317 ± 0.001	0.011 ± 0.001	-0.165 ± 0.001	-0.021 ± 0.001
	$\mathcal{G}_{ref}$	0.441 ± 0.002	0.0140 ± 0.0004	-0.145 ± 0.003	-0.024 ± 0.001
0.5	$\mathcal{H}_{ref}$	0.313 ± 0.001	0.0100 ± 0.0003	-0.174 ± 0.001	-0.021 ± 0.001
	$\mathcal{G}_{ref}$	0.436 ± 0.001	0.014 ± 0.001	-0.165 ± 0.002	-0.024 ± 0.001

| z | Sample | $\xi_\perp(s_{ref})$ | | $\xi_\parallel(s_{ref})$ | |
		$16h^{-1}$ Mpc	$64h^{-1}$ Mpc	$16h^{-1}$ Mpc	$64h^{-1}$ Mpc
0	$\mathcal{H}_{ref}$	0.261 ± 0.001	0.0040 ± 0.0004	0.367 ± 0.001	0.0180 ± 0.0004
	$\mathcal{G}_{ref}$	0.408 ± 0.002	0.490 ± 0.001	0.490 ± 0.002	0.023 ± 0.001
0.3	$\mathcal{H}_{ref}$	0.255 ± 0.001	0.0030 ± 0.0004	0.379 ± 0.001	0.0190 ± 0.0004
	$\mathcal{G}_{ref}$	0.387 ± 0.002	0.496 ± 0.001	0.496 ± 0.002	0.023 ± 0.001
0.5	$\mathcal{H}_{ref}$	0.248 ± 0.001	0.0020 ± 0.0004	0.378 ± 0.001	0.0180 ± 0.0004
	$\mathcal{G}_{ref}$	0.374 ± 0.002	0.498 ± 0.001	0.498 ± 0.002	0.023 ± 0.001

where a ratio between 2PCFs of different halo populations at a chosen scale was studied. In that work, the relative clustering ratio $\mathcal{R}$ for the monopole of the 2PCF of halo populations was introduced. Taking the ratio of the two amplitudes of 2PCFs eliminates the linear bias contribution to the first order. Here we extend that definition to the quadrupole moment and clustering wedges of the 2PCF. This will allow us to look for signatures of MG encoded also in the higher-order multipole moments of the anisotropy produced by RSD.

The clustering ratio of multipole moments of order l, or clustering wedges w, $\mathcal{R}_{l,w}$, is defined as follows:

$$\mathcal{R}_{l,w}(s, \mathcal{H}|\mathcal{H}_{ref}, s_{ref}) = \frac{s^2 \xi_{l,w}(s|\mathcal{H})}{s_{ref}^2 \xi_{l,w}(s_{ref}|\mathcal{H}_{ref})}, \quad (20)$$

where $\mathcal{H}_{ref}$ is a reference halo (galaxy) sample, and s_{ref} is a fixed reference (comoving) scale. The choice of the reference halo/galaxy sample should be made in a way to minimize the effect of noise. In general, a population with the highest abundance would seem best suited here. However, in the case of data from real galaxy surveys, an optimal galaxy population could be the one with the best completeness or the largest sky coverage. Nevertheless, in our calculations, we use uniformly selected halo and galaxy samples considered in a distant observer approximation. Thus, we opt for a simple criterion of the highest sampling rate for our choice of the reference halo population, i.e., in our case, $\mathcal{H}_{ref} = \mathcal{H}_1$ of number density $\bar{n} = 10^{-3}h^3$ Mpc^{-3}.

Since we deal with only one galaxy sample, it will requite special treatment. The reference and target populations will be identical, so the clustering ratios will reduce to a normalization of the signal by its amplitude at the reference scale $s = s_{ref}$. This will also be the case whenever we compute $\mathcal{R}$ for the reference halo sample itself. Therefore, in

all these cases, the relative clustering maximizes the differences between the MG models depending on the reference scale s_{ref}. In what follows, we explore the behavior of the relative clustering ratios by considering two different reference scales, i.e., $s_{ref} = 16$ and $64h^{-1}$ Mpc. These are the same values as used by [53]. Table IV gives the amplitudes of the multipole moments (top) and clustering wedges (bottom) of the 2PCF for GR at these reference scales. The four panels of Fig. 10 show the relative differences in the clustering ratio for the monopole $\mathcal{R}_0$ (left-hand panels) and the quadrupole $\mathcal{R}_2$ (right-hand panels) for all our halo and galaxy samples taken at the discussed reference scales, upper panels for $s_{ref} = 16$ and lower panels for $64h^{-1}$ Mpc. Similarly, Fig. 11 displays the relative difference between the clustering ratio defined for wedges, parallel $\mathcal{R}_\parallel$ (left-hand panels) and transverse $\mathcal{R}_\perp$ (right-hand panels), again for $s_{ref} = 16$ at the top and $64h^{-1}$ Mpc at the bottom.

The analysis of the generalized clustering ratio that we have introduced in Eq. (20) leads to interesting conclusions. In general, no single ratio is the "smoking gun" for the MG imprint and various models exhibit beyond-GR signals, if any, in various statistics and for different tracer populations. Looking first at Fig. 10, for the monopole ratio $\mathcal{R}_0$, we see that for the $\mathcal{H}_3$ halos both F5 and N1 show clear deviations with respect to ΛCDM of $\sim -5\%$, for both reference scales. Some signal can be also observed for these models in $\mathcal{H}_2$ for $s_{ref} = 16h^{-1}$ Mpc, and for N1 only in the $\mathcal{H}_2$ and $\mathcal{G}$ tracers if $s_{ref} = 64h^{-1}$ Mpc. Also the F6 model exhibits some departures from GR in this statistic, namely for $\mathcal{H}_2$ and $\mathcal{H}_3$ for the smallest reference scale, and for $\mathcal{G}$ with the $64h^{-1}$ Mpc reference. For all other combinations of MG models, tracers, and reference scales, the differences in $\mathcal{R}_0$ with respect to ΛCDM are mostly within the statistical noise.
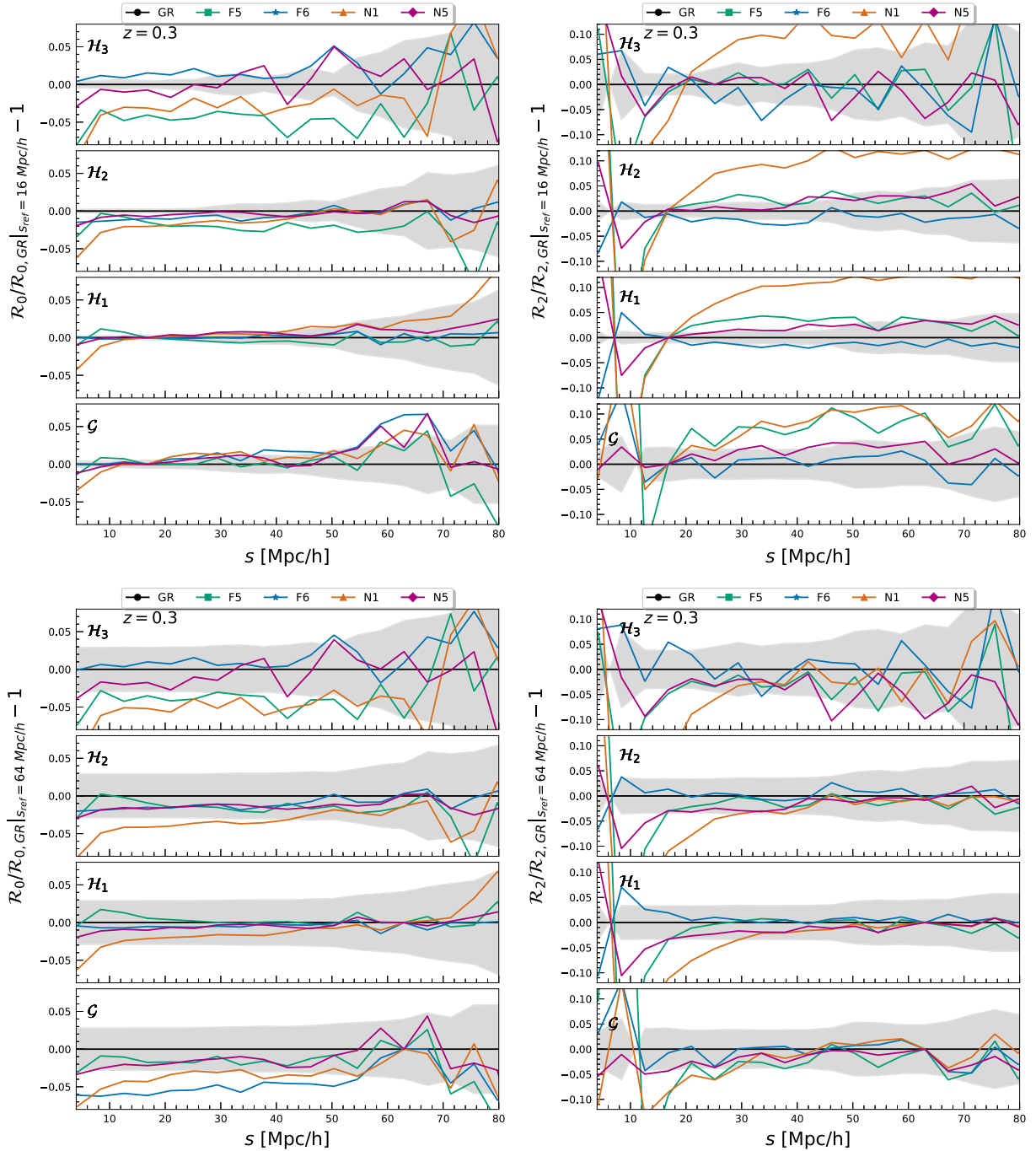
FIG. 10. Relative difference of the MG clustering ratios with respect to the ΛCDM measurements for both the monopole (left) and quadrupole (right) of the 2PCF of halos (galaxies), as indicated by the labels, at two different reference scales $s_{\rm ref} = 16h^{-1}$ Mpc (upper panels) and $s_{\rm ref} = 16h^{-1}$ Mpc (lower panels). The gray-shaded areas correspond to the standard deviation for GR over 15 measurements of the 2PCF estimation.

The quadrupole clustering ratio $\mathcal{R}_2$ seems to be less sensitive than $\mathcal{R}_0$ as a discriminant of gravity models. For the $64h^{-1}$ Mpc reference scale, most of the MG model-population combinations do not show differences from GR that would stand out from statistical scatter, only N1 offers

a strong signal at $20 < s[h^{-1}\ {\rm Mpc}] < 30$. The situation is better for $s_{\rm ref} = 16h^{-1}$ Mpc, where for all the tracer populations, the N1 model exhibits significant, of $\sim + 10\%$ or larger, deviations from ΛCDM in this statistic. For $\mathcal{G}$, $\mathcal{H}_1$, and (less significantly) $\mathcal{H}_2$, also N5 could be
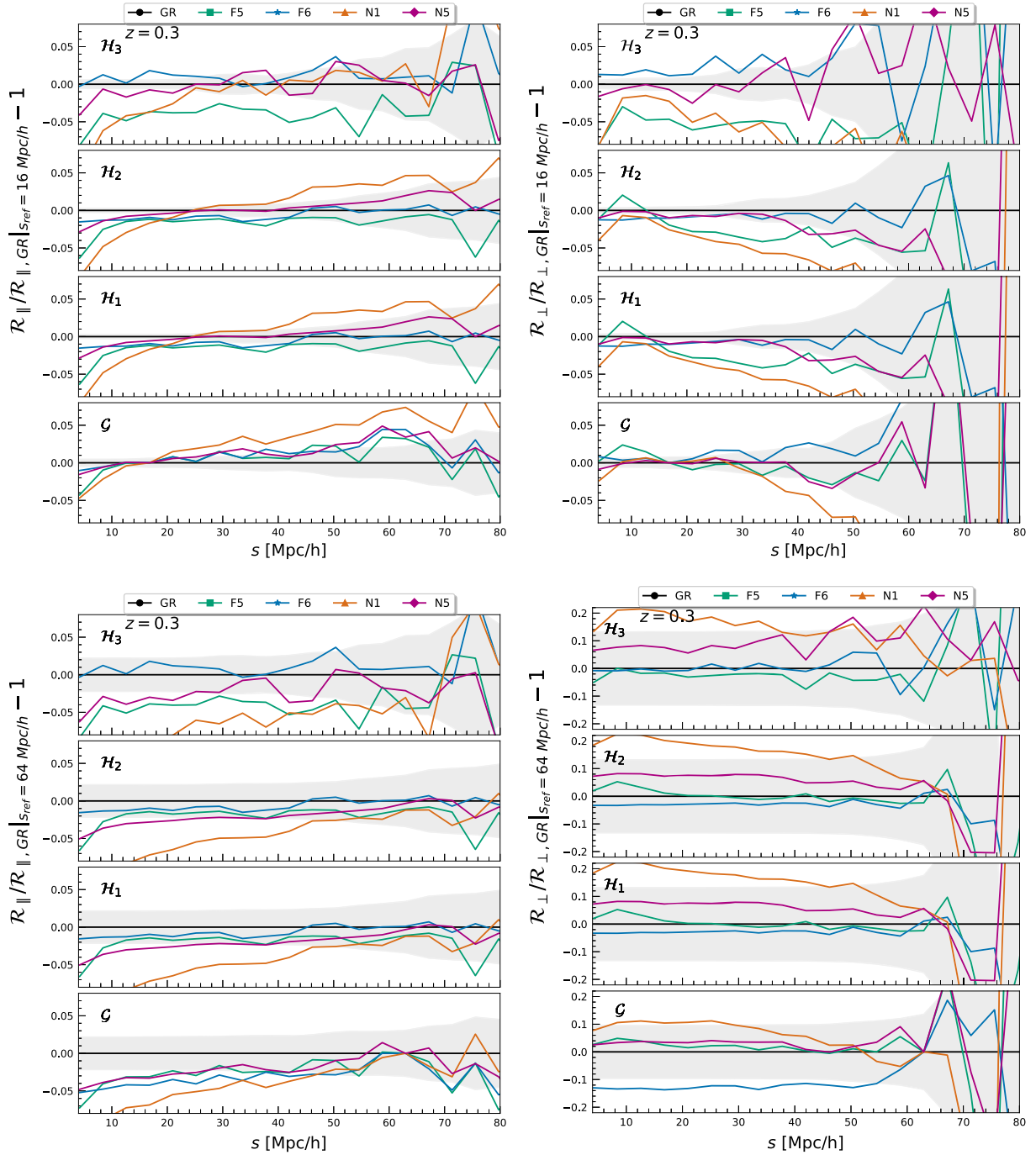
FIG. 11.   Same as Fig. 10 but for the ratios of the redshift-space clustering wedges (parallel and perpendicular) of the 2PCF.

possibly discriminated from GR using $\mathcal{R}_2$ with the smaller reference scale; in fact, for galaxies, the signal is in this case of the same strength for both the nDGP models. Some signal is visible also for F6 for the middle tracer populations ($\mathcal{H}_1$ and $\mathcal{H}_2$), but its amount of $\sim -2\%$ is hardly outside the statistical errors.

In Fig. 11 we illustrate the differences between MG and GR for the clustering ratios computed for the parallel and

perpendicular redshift-space wedges. For both wedge types and the two reference scales, N1 generally departs from GR by several percent, although there are exceptions for some of the populations where the signal is not significant. While the mass selection of $\mathcal{H}_3$ seems to be make it possible to distinguish the effects of MG in the F5 model, which departs from GR by up to 5% up to $60h^{-1}$ Mpc, for the denser samples this is no longer possible in general,

therefore, this behavior is somewhat reverse with respect to N1. Furthermore, the ratio of the parallel wedge evaluated for both reference scales shows that the relative differences of the clustering of N5 increase monotonically with scale, while these appreciable differences do not appear in the conventional analysis of wedges when comparing with respect to the ΛCDM model. Next, for the clustering ratio of the transverse wedge, it is not efficient to use a large reference scale $s_{\mathrm{ref}} = 64h^{-1}$ Mpc to disentangle the screening effects of modifications of gravity. Although the relative clustering attempts to eliminate the dependence on the linear bias in the correlations, the F6 model shows a trend that tracks closely the standard model, not being distinguishable even when the densest halo population is considered. This means there are other features of the structure growth predicted by MG models, especially in $f(R)$-based models such as F6, that are strongly degenerate with ΛCDM and that do not allow us to unveil the effects of modified gravity with RSD, and we cannot even fully remove the issue of the linear bias when using the clustering ratios.

A. Estimation of β from clustering ratios

We propose a new estimator for the redshift-space distortion parameter β based on linear theory results and the above-introduced relative clustering ratio, given a reference sample and scale. It is defined via the following equation:

$$
\begin{aligned}
P(s) &= \frac{\xi_{\mathrm{DM}}(r)}{\xi_{\mathrm{DM}}(r_{\mathrm{ref}})} \frac{\beta_{\mathrm{ref}}^2(s)}{1 + \frac{2}{3}\beta_{\mathrm{ref}} + \frac{1}{5}\beta_{\mathrm{ref}}^2} \frac{s^2}{s_{\mathrm{ref}}^2 \mathcal{R}_0(s)}, \\
&= \frac{\xi_{\mathrm{DM}}(r)}{\xi_{\mathrm{DM}}(r_{\mathrm{ref}})} \frac{\beta_{\mathrm{ref}}^2(s)}{R(\beta_{\mathrm{ref}}, s)} \frac{s^2}{s_{\mathrm{ref}}^2 \mathcal{R}_0(s)}.
\end{aligned} \tag{21}
$$

Here, $R(s)$ is given by Eq. (16), and this $P(s)$ estimator is an extension of the Q and R statistics discussed in Sec. IV. Although, for a theoretical analysis, the real space 2PCF can be obtained from Boltzmann solvers that implement HALOFIT [146], such as CAMB [147] or CLASS [148]; we focus instead on the expected values that can be measured from observables in redshift space. The real-space contribution in Eq. (21) can be canceled out by evaluating $P(s)|_{s_{\mathrm{ref}}}$, which gives:

$$
P(s)|_{s_{\mathrm{ref}}} \equiv \frac{\beta_{\mathrm{ref}}^2}{R(\beta_{\mathrm{ref}})} \frac{1}{\mathcal{R}_0(s_{\mathrm{ref}})} = \frac{\beta^2}{R(\beta)}. \tag{22}
$$

As P can be obtained directly from the measured 2PCF, this provides a natural scaling of the distortion parameter for MG cosmologies, both for halo and galaxy samples. As the main consequence of implementing the P estimator, we highlight that the accuracy in the resulting β value for a given number density, different from the reference sample, will depend strongly on how well $\beta_{\mathrm{ref}} \equiv \beta(s_{\mathrm{ref}}, \mathcal{H}_{\mathrm{ref}})$ is
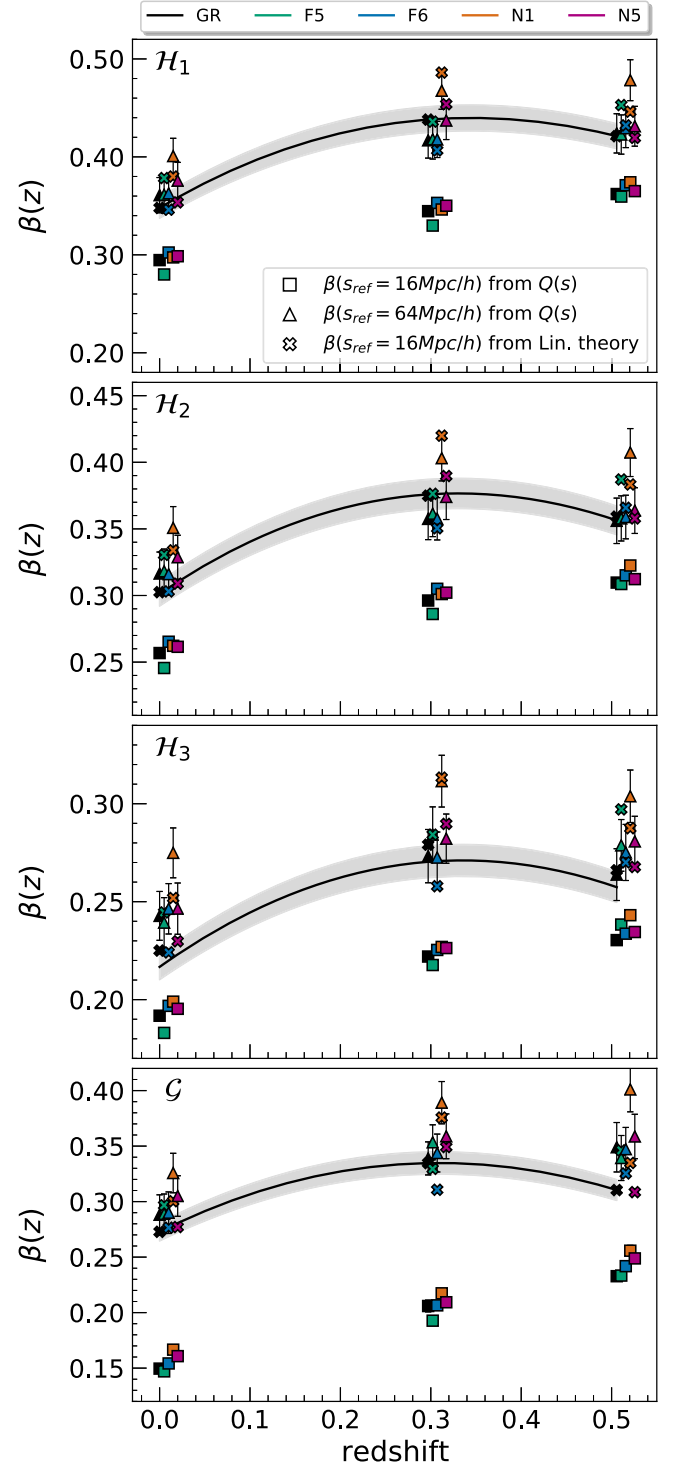

FIG. 12. Linear distortion parameter $\beta(z)$ obtained from the clustering ratios of halos (galaxies). The different symbols correspond to different β_{ref} values used in the P estimator Eq. (22), as illustrated in the legend. For better visualization, the redshift of the MG models has been shifted from the mean values $z = 0$, 0.3, and 0.5. The solid line shows the theoretical ΛCDM prediction computed according to Tinker *et al.* [138]. The error bars represent propagated statistical noise and the gray-shaded areas show a 3% error for reference.

constrained, i.e., the distortion parameter obtained from the reference sample and scale. Figure 12 shows the linear distortion parameter obtained from the P estimator, for all MG models and samples, in both reference scales in which the clustering ratio was evaluated, i.e., $s_{\rm ref} = 16$ and $64h^{-1}$ Mpc, as well as for the linear prediction, as indicated by the different symbols. As previously pointed out in Sec. VI, the $\mathcal{H}_1$ population exhibits self-consistent results since it corresponds to the reference sample.

For all tracers, using $\beta_{\rm ref}$ for $s_{\rm ref} = 16h^{-1}$ Mpc leads to significantly underestimated β, when compared to the linear theory. This effect gets more pronounced at low redshifts $z \le 0.3$. The amount of this bias varies from up to 45% for the galaxy population, down to 15% for $\mathcal{H}_3$. This underestimation is not surprising, as at $16h^{-1}$ Mpc the amplitudes of the 2PCF are significantly affected by the FOG effect and other potential issues connected to small nonlinear scales. Since we do not attempt to model the velocity damping term, our estimation of linear-theory β using the $P(s)$ estimator must give a result biased low. In contrast, using $\beta_{\rm ref}$ for $s_{\rm ref} = 64h^{-1}$ Mpc yields much more self-consistent results. This is expected since the impact of the random virialized motions of halos and galaxies onto the clustering is much weaker at those scales when compared to the weakly nonlinear regime at $16h^{-1}$ Mpc [22,127,149].

Assuming that all the relevant effects are modeled precisely, the P-based estimator for β would foster a significant measurement of the distortion parameter. In principle, it would offer precision that should allow to distinguish between ΛCDM and at least the F5 and N1 models. We can emulate such a situation by using a linear-theory prediction for each model as our $\beta_{\rm ref}$. In that case, we obtain a much better accuracy of the extracted $\beta(z)$ than from the $Q(s)$ measurements. Of course, an actual real-data measurement cannot assume a value of the parameter that is to be measured. However, our exercise with taking $\beta_{\rm ref} \equiv \beta_{\rm linear}$ illustrates a theoretical accuracy limit, which one can approach by carefully modeling all the relevant nonlinear effects, such as velocity damping and scale-dependent galaxy bias. This will be explored in future work.

VII. DISCUSSION

In this paper we have performed a systematic search for modified gravity signals that would be encoded in various halo and galaxy clustering statistics. Starting from linear theory, we considered a set of basic predictions, such as halo mass function, linear growth rate parameter, and effective linear bias. We have employed a set of N-body simulations, the ELEPHANT suite, and used mock halo and galaxy catalogs to construct three halo ($\mathcal{H}_{1,2,3}$) and one galaxy ($\mathcal{G}$) samples. We then proceeded to measure the full 2D two-point correlation function using a distant observer approximation for redshift-space distortions modeling.

Next, we have studied various moments of the full 2D 2PCF and other related statistics against their potential sensitivity to the underlying gravity model. Our main focus was on the $z = 0.3$ snapshot. This epoch, from all the available snapshots, should be the closest representation of the BOSS LOWZ ($z \lesssim 0.4$) data, the characteristics of which were used to construct galaxy mock catalogs in ELEPHANT. We can summarize our most important findings as follows.

A. Clustering in the real space

The amplitudes of the matter 2PCF and power spectrum are enhanced in MG models, compared to the GR baseline prediction. This is a result of a continued action of the fifth force on the DM fluid. The net effect seen in simulations agrees well with the enhancement of the linear growth-rate parameter as predicted from the perturbation theory. However, this effect is not translated straightforwardly to the measured galaxy and halo 2PCFs. We have shown that here the additional factors, like biasing and population selection criteria, affect the resulting correlation amplitudes. These all add up to produce sometimes counter-intuitive or surprising results. For example, the N1 model is characterized by an excess over the ΛCDM amplitude for $\mathcal{H}_1$ and $\mathcal{H}_2$ samples but shows no significant difference for $\mathcal{H}_3$ and $\mathcal{G}$. In contrast, the F5 model predicts weaker clustering for the $\mathcal{H}_2$ sample, while for all the other populations it is close to GR predictions. In addition, there is no clear trend with the MG signal and the sample density; as for the F5 case, our sparsest population $\mathcal{H}_3$ can exhibit similarly strong deviations as N1 for $\mathcal{H}_1$. For all models, the galaxy sample exhibits a clustering amplitude consistent with each other with a typical scatter of 1–2%. This result is expected, as by construction the amplitude of the projected correlation function was enforced when building the HOD mocks. The overall picture emerging from our analysis of the real-space clustering points to significant nonlinear behavior across various samples and models. This emphasizes the need to use carefully designed simulations for predicting halo and galaxy clustering in MG.

B. Halo and galaxy bias

Our study clearly shows that the linear bias parameter in MG can differ significantly from the GR one for mass-selected samples. The departure from GR of the linear bias at the fixed halo mass has been already indicated by previous studies [see, e.g., [49,50,149,150]]. Here, we also showed that the effective bias, representative of the fixed number-density samples, varies across models for the same sample selection. Our results also confirm that for all the studied MG models, as well as for the GR case, the scale dependence of the linear bias is weak. The resulting relative differences of the bias with respect to ΛCDM is also relatively flat and only slightly changing with scale. The F5 model is a clear exception here, however.

The deviation of the F5 bias for all but $\mathcal{H}_3$ samples experiences visible nonlinear scale dependence. Noticeably, for this $f(R)$ model the bias usually takes values higher than in ΛCDM. In contrast, for the N1 case it is always lower than for GR for all our samples. F6 and N5 show much smaller differences that are typically not significant, given the scatter. We also studied the redshift evolution of the bias parameter in the range of $0 < z < 0.5$. We found that the differences from GR are larger at higher redshift, indicating that bias modeling accounting for MG-related physics should be really important for all $z > 0$ galaxy data.

In general, we find that the bias of galaxy and halo samples can take significantly different values in MG than in the fiducial ΛCDM model. The net effect can have both positive and negative signs and additionally depends on the sample number density. This indicates that there is an important degeneracy between the enhanced structure formation, as predicted by the increased growth rate of MG models, and their bias values, different than in GR. This degeneracy needs to be carefully considered in all MG growth-rate measurements employing biased tracers, and therefore, its impact on the growth-rate estimation must be eliminated or at least minimized.

C. Clustering in the redshift space

The isocorrelation contours of the MG 2D 2PCF exhibit visible deviations from the GR case for the three halo samples. For the case of the galaxy sample, the deviations of the contour lines are much milder than in GR. The modulation of MG effects with the changing number density, from $\mathcal{H}_3$ to $\mathcal{H}_1$ samples, highlights that the amplitude of real space clustering varies more in the transverse than the LOS direction.

1. Monopole moment of the 2PCF

We find that the clustering amplitudes of the $\mathcal{H}_2$ and $\mathcal{G}$ samples are very close to each other when paired consistently for all MG models. This results in very similar, albeit not identical, trends of departures from GR in those two samples. For all samples, N1 shows a clustering excess in the $\xi_0(s)$ amplitude at all probed scales. The magnitude of this excess is also correlated with the number density of the sample. The signal for N5 follows qualitatively the same trends but with moderately smaller excess amplitude. The $f(R)$ family exhibits quite different behavior. Here, typically the monopole amplitude takes lower values than in the ΛCDM case. However, the F5 model for the $\mathcal{H}_1$ sample departs from this trend as $\xi_0(s)$ takes here values higher than GR. For the nDGP models, the observed excess of the clustering amplitude is relatively flat with scale, while the $f(R)$ family show some weak scale dependence, with smaller scales usually showing a stronger signal. We can attribute this latter behavior to the chameleon screening

mechanism that, due to its environmental dependence, adds additional variability with scale in this class of models.

2. Quadrupole moment of the 2PCF

The analysis of the quadrupole moments yields one clear prediction: only the N1 model shows a signal of deviation from GR that is strong and statistically significant. The net amplitude boost is quite large and takes up to 20% for all four samples. N5 also shows some deviations, but they are much more minor in the amplitude and hence only marginally significant. Both of our $f(R)$ variants show virtually no signal here, as their quadrupole moments take values that are very close to the fiducial GR case.

3. Clustering wedges

The signal of the MG-enhanced structure formation appears to be better visible in the analysis of the clustering wedges than of the multipoles. The net effect on the amplitude boost of the LOS wedge reaches 10% and 5% for N1 and N5 variants, respectively. The significance of this signal is also prominent since the statistical uncertainty levels remain comparable with the one for the monopoles. This shows promise of using the LOS clustering wedges for rendering stronger constraints on the nDGP class of models. On the other hand, for the perpendicular sky direction, the galaxy sample was much less sensitive to MG effects. The effect was still prominently present in the halo samples but now contained only to small nonlinear scales. Thus, we argue that the perpendicular clustering wedge is not well suited for testing growth-rate deviations. Interestingly, for both parallel and perpendicular wedges the amplitudes for $f(R)$ samples are close to the ΛCDM case, deviating by no more than ∼2%. These indicate that the wide-angle integration over the 2D 2PCF results in a statistic that is rather insensitive to the $f(R)$-model effects.

4. Linear distortion parameter β

Our measurements of $\beta(z)$ performed with the quadrupole-based estimator $Q(s)$ clearly illustrate that the beyond-GR modified bias and the modified growth rate are combined in a way that is not straightforward to model nor account for it, at best. In the case of N1, where the increased $f(z)$ is accompanied by a decrease of the galaxy/halo bias, the net effect on $\beta(z)$ is always positive. This is reflected in the estimated β values that clearly, for all redshifts and samples, lie systematically above the ΛCDM case. The N5 model should, in principle, exhibit a similarly combined trend, but the net effect is small given our statistical uncertainties. Therefore, our results here are only offering a hint in this direction.

For both $f(R)$ variants we find, however, that the resulting distortion parameter for all samples and redshifts is always very close to the fiducial GR case. The weak and nonsignificant result for F6 is actually expected as this

model, in general, is characterized by only a very weak departure from the GR structure formation. For the F5 model, the increased bias conspires against the enhanced growth rate. In this case the total effect brings β values much closer to the ΛCDM scenario. This might be somewhat surprising given the fact that the F5 variant in the linear regime deviates rather significantly from GR.

The overall picture emerging is this: while the quadrupole growth rate estimator offers good sensitivity to the nDGP models, it performs very poorly as a method to differentiate between GR and F5 or F6.

D. Measurements of the clustering ratios

The relative clustering ratios promise to be less susceptible to the growth rate-bias degeneracy, as revealed by our analysis of the estimators based on correlation function moments. This is related to the fact that, in the ratio, the effect of the first-order linear bias contribution is reduced.

1. Ratios of multipole moments

The analysis revealed that the smaller of our two reference scales, i.e., $16h^{-1}$ Mpc, in general, fosters bigger differences of the MG clustering ratios versus the ΛCDM case than for $s_{\rm ref} = 64h^{-1}$ Mpc. For halos, on top of the notoriously strong signal of N1, only the monopole ratio taken from the $\mathcal{H}_3$ population contained a significant signal for another model, F5 in this case. We find, however, a very promising result for the galaxy population and the quadrupole ratios. In this case, both N1 and F5 are characterized by a clear and significant signal attaining nearly a $\sim 10\%$ difference from GR with $\sim 2\sigma$ significance. The results taken for the reference scale at $64h^{-1}$ Mpc are characterized by a much bigger scatter. This has diminished the significance of nearly all the signals, with two notable exceptions for the monopole ratios of $\mathcal{H}_3$ and $\mathcal{G}$ samples. The $\mathcal{H}_3$ population of N1 and F5 models presents a $\sim 5\%$ deviation but with a marginal 1σ significance. Among the exciting results for the galaxy sample, we find a clear signal of 5% for the F6 model with statistical significance $\geq 1.5\sigma$, which emerges at $s \lesssim 40h^{-1}$ Mpc for $\mathcal{R}_0$. The $\mathcal{G}$ sample yields also marginally significant deviation for N1 at the 3% level.

2. Ratios of clustering wedges

The landscape is largely similar for the case of the clustering wedge ratios. Although the MG effects are now typically smaller at $s_{\rm ref} = 16h^{-1}$ Mpc than at $64h^{-1}$ Mpc, the significance behaves actually inversely. From the combination of the scales and models, we showed that the ratios of the clustering wedges can actually accommodate significant deviations for N1 and F5 MG variants. Looking at smaller scales, also the F6 and N5 models manifest departures from GR. Here, an especially interesting aspect is a large deviation of 12% deviation pertaining

for scales up to $50h^{-1}$ Mpc that the F6 model shows in the galaxy sample. This signal maintains a nearly 1σ significance for all the scales.

3. Estimation of $\beta(z)$

Using the definition of the clustering ratios, we have formulated a new estimator for β based on the ratio of two monopoles in redshift space, i.e., $\mathcal{R}_0$. Applying this estimator for ratios taken at $s_{\rm ref} = 64h^{-1}$ Mpc results in a similar performance, as in the case of the standard Q-based β-estimator. For the small reference scale $s_{\rm ref} = 16h^{-1}$ Mpc, the distortion parameter values are largely underestimated, which indicates that the nonlinear effects at those scales, both in the velocity and the density field, are significant. Ignoring this leads to a severe bias in the β-parameter estimation. Using additional information, in our case the value of the linear-theory predicted $\beta_{\rm ref}$, greatly improves the accuracy and the performance of the new estimator. Now, for most redshifts and samples the results for all MG variants are clearly separated; this illustrates the power of more thorough modeling. Using the linear theory prediction allows one to break the bias-growth-rate degeneracy. This exercise yields, therefore, a theoretical maximal sensitivity of the $\mathcal{R}_0$-based estimator, which could be achieved in the case of accurate small-scale modeling. This modeling would potentially include scale-dependent nonlinear bias and velocity damping.

VIII. CONCLUSIONS

The enhanced structure formation, fostered to a various degree by all MG scenarios we considered, leads to clear predictions in the linear regime. However, the presence of highly nonlinear fifth-force screening mechanisms, i.e., the Vainshtein and the chameleon effects, in general, increase significantly the total degree of nonlinearity in such scenarios. Our analysis of the redshift-space clustering of four different samples across five variants of structure formation scenarios clearly confirms that there is rich potential in using such clustering statistics, both for testing the self-consistency of GR, as well as for searching for alternative MG signals. We have unveiled MG signals present in the various statistics, such as multipole moments, clustering wedges, and clustering ratios, across our halo and galaxy samples. Similar results for some of the statistics considered here were previously found by other authors [see, e.g., [47–49,51,53,54,85,88]].

The deviations from the GR baseline of the various clustering statistics should manifest themselves as measurable differences in the linear growth-rate f. A common procedure to measure it involves extracting the $f\sigma_8$ product from the best-fit model of the data. This combination is treated as a convenient single parameter to be compared across different data sets and different models. What is actually measured, however, is $\beta\sigma_8^G$, a product of the linear

distortion parameter normalized by a given galaxy sample linear variance σ_8^G, taken at $s = 8h^{-1}$ Mpc. Therefore, marginalization over $b\sigma_8$ needs to be done in order to obtain an $f\sigma_8$ measurement. Our analysis is indicating potential dangers of this procedure if the resulting constraints on $f\sigma_8$ are to be used for testing gravity. Due to highly nonlinear behavior of tracer bias in modified gravity, especially in the case of chameleon $f(R)$ theories, such naive marginalization may lead to a biased $f\sigma_8$ result. Only when the scale dependence of MG, GR bias, and other sources of degeneracy are well mapped, can a comparison of $f\sigma_8$ for different gravity models and galaxy samples be regarded as self-consistent and free of severe systematics.

The effective galaxy/halo bias in the MG models we studied here can differ from the GR baseline by at least $\sigma_b/b_{MG} \simeq \pm 0.05$. Such variability, if unaccounted for, will add a systematic effect into the growth-rate measurement. A robust study based on high-resolution simulations for each inquired MG model is needed to chart the growth-rate-bias degeneracy and add such modeling into $f\sigma_8$ determination. In case such robust modeling is not yet available for a given MG model, we advocate a safer approach consisting of using the linear distortion parameter instead. In addition, $\beta(z)$ can be readily measured for each galaxy sample separately and used for constraining and comparing GR and MG consistently within the given dataset. The trade-off is that the resulting β parameter is less sensitive to a modified growth rate in the models, where the galaxy bias can be modified in a nonlinear way, such as $f(R)$. When

dealing with models that accommodate more predictive bias modifications, such as the nDGP class, $\beta(z)$ already could be used for obtaining robust constraints on strongly deviating variants, such as N1 tested here. If the nuisances are controlled and viably modeled, this parameter can yield competitive constraints on MG models from the current and, especially, future spectroscopic galaxy surveys.

Our study also indicates that smaller scales contain much more constraining power when using RSD for testing gravity. While this is a relatively well-known and appreciated fact for the case of the standard ΛCDM analysis, it is even more vital to tap the small-scale potential for conducting competitive and stringent MG tests with the use of clustering data. A natural next step to exploit this potential would be a systematic study of the nonlinear small-scale bias and the effects of galaxy pairwise velocity dispersion in the context of RSD and MG physics. Such a program is already underway, and we will present its results in a forthcoming study.

[1] E. Semboloni *et al.*, Astron. Astrophys. **452**, 51 (2006).
[2] M. Hamuy *et al.*, Publ. Astron. Soc. Pac. **118**, 2 (2006).
[3] G. Miknaitis *et al.*, Astrophys. J. **666**, 674 (2007).
[4] A. Conley *et al.*, Astrophys. J. Suppl. Ser. **192**, 1 (2011).
[5] S. Alam *et al.*, Mon. Not. R. Astron. Soc. **470**, 2617 (2017).
[6] Planck Collaboration, Astron. Astrophys. **641**, A1 (2020).
[7] P. J. E. Peebles and B. Ratra, Rev. Mod. Phys. **75**, 559 (2003).
[8] S. Sarkar, Gen. Relativ. Gravit. **40**, 269 (2008).
[9] J. A. Frieman, M. S. Turner, and D. Huterer, Annu. Rev. Astron. Astrophys. **46**, 385 (2008).
[10] P. Brax, Rep. Prog. Phys. **81**, 016902 (2018).
[11] M. Kramer *et al.*, Science **314**, 97 (2006).
[12] J. P. Uzan, Phil. Trans. R. Soc. A **369**, 5042 (2011).
[13] C. M. Will, Living Rev. Relativity **17**, 4 (2014).
[14] T. E. Collett, L. J. Oldham, R. J. Smith, M. W. Auger, K. B. Westfall, D. Bacon, R. C. Nichol, K. L. Masters, K. Koyama, and R. van den Bosch, Science **360**, 1342 (2018).
[15] B. P. Abbott *et al.* (The LIGO Scientific Collaboration and the Virgo Collaboration), Phys. Rev. D **100**, 104036 (2019).
[16] S. Capozziello and M. de Laurentis, Phys. Rep. **509**, 167 (2011).
[17] K. Koyama and F. P. Silva, Phys. Rev. D **75**, 084040 (2007).
[18] T. P. Sotiriou and V. Faraoni, Rev. Mod. Phys. **82**, 451 (2010).
[19] A. De Felice and S. Tsujikawa, Living Rev. Relativity **13**, 3 (2010).
[20] R. Maartens and K. Koyama, Living Rev. Relativity **13**, 5 (2010).
[21] A. J. S. Hamilton, *Linear Redshift Distortions: A Review* (Springer Netherlands, Dordrecht, 1998), pp. 185–275.
[22] R. Scoccimarro, Phys. Rev. D **70**, 083007 (2004).
[23] A. Taruya, K. Koyama, T. Hiramatsu, and A. Oka, Phys. Rev. D **89**, 043509 (2014).
[24] M. Ishak, Living Rev. Relativity **22**, 1 (2019).

[25] P. G. Ferreira, Annu. Rev. Astron. Astrophys. **57,** 335 (2019).

[26] T. Baker et al., Rev. Mod. Phys. **93,** 015003 (2021).

[27] V. Desjacques, D. Jeong, and F. Schmidt, Phys. Rep. **733,** 1 (2018).

[28] L. Verde et al., Mon. Not. R. Astron. Soc. **335,** 432 (2002).

[29] J. C. Jackson, Mon. Not. R. Astron. Soc. **156,** 1P (1972).

[30] N. Kaiser, Mon. Not. R. Astron. Soc. **227,** 1 (1987).

[31] R. Laureijs et al., arXiv:1110.3193.

[32] DESI Collaboration, arXiv:1611.00036.

[33] P. J. E. Peebles, The Large-Scale Structure of the Universe (Princeton University Press, Princeton, NJ, 1980).

[34] K. B. Fisher, Astrophys. J. **448,** 494 (1995).

[35] A. Taruya, T. Nishimichi, and S. Saito, Phys. Rev. D **82,** 063522 (2010).

[36] L. F. de la Bella, D. Regan, D. Seery, and S. Hotchkiss, J. Cosmol. Astropart. Phys. 11 (2017) 039.

[37] Y.-S. Song, Y. Zheng, A. Taruya, and M. Oh, J. Cosmol. Astropart. Phys. 07 (2018) 018.

[38] K. Koyama, A. Taruya, and T. Hiramatsu, Phys. Rev. D **79,** 123512 (2009).

[39] B. Bose and K. Koyama, J. Cosmol. Astropart. Phys. 08 (2016) 032.

[40] A. Taruya, Phys. Rev. D **94,** 023504 (2016).

[41] B. Bose, K. Koyama, W. A. Hellwing, G.-B. Zhao, and H. A. Winther, Phys. Rev. D **96,** 023519 (2017).

[42] A. Barreira, S. Bose, and B. Li, J. Cosmol. Astropart. Phys. 12 (2015) 059.

[43] S. Bose, B. Li, A. Barreira, J.-H. He, W. A. Hellwing, K. Koyama, C. Llinares, and G.-B. Zhao, J. Cosmol. Astropart. Phys. 02 (2017) 050.

[44] C. Arnold, M. Leo, and B. Li, Nat. Astron. **3,** 945 (2019).

[45] H. A. Winther, K. Koyama, M. Manera, B. S. Wright, and G.-B. Zhao, J. Cosmol. Astropart. Phys. 08 (2017) 006.

[46] C. Arnold, P. Fosalba, V. Springel, E. Puchwein, and L. Blot, Mon. Not. R. Astron. Soc. **483,** 790 (2019).

[47] E. Jennings, B. Li, C. M. Baugh, K. Koyama, and G.-B. Zhao, Mon. Not. R. Astron. Soc. **425,** 2128 (2012).

[48] F. Marulli, M. Baldi, and L. Moscardini, Mon. Not. R. Astron. Soc. **420,** 2377 (2012).

[49] M. Wyman, E. Jennings, and M. Lima, Phys. Rev. D **88,** 084029 (2013).

[50] A. Barreira, A. G. Sánchez, and F. Schmidt, Phys. Rev. D **94,** 084022 (2016).

[51] S. Alam et al., arXiv:2011.05771.

[52] M. Cautun, E. Paillas, Y.-C. Cai, S. Bose, J. Armijo, B. Li, and N. Padilla, Mon. Not. R. Astron. Soc. **476,** 3195 (2018).

[53] P. Arnalte-Mur, W. A. Hellwing, and P. Norberg, Mon. Not. R. Astron. Soc. **467,** 1569 (2017).

[54] C. Hernández-Aguayo, J. Hou, B. Li, C. M. Baugh, and A. G. Sánchez, Mon. Not. R. Astron. Soc. **485,** 2194 (2019).

[55] T. Clifton, P. G. Ferreira, A. Padilla, and C. Skordis, Phys. Rep. **513,** 1 (2012).

[56] A. Joyce, B. Jain, J. Khoury, and M. Trodden, Phys. Rep. **568,** 1 (2015).

[57] P. Creminelli and F. Vernizzi, Phys. Rev. Lett. **119,** 251302 (2017).

[58] T. Baker, E. Bellini, P. G. Ferreira, M. Lagos, J. Noller, and I. Sawicki, Phys. Rev. Lett. **119,** 251301 (2017).

[59] W. Hu and I. Sawicki, Phys. Rev. D **76,** 064004 (2007).

[60] G. Dvali, G. Gabadadze, and M. Porrati, Phys. Lett. B **485,** 208 (2000).

[61] A. I. Vainshtein, Phys. Lett. **39B,** 393 (1972).

[62] E. Babichev and C. Deffayet, Classical Quantum Gravity **30,** 184001 (2013).

[63] J. M. Ezquiaga and M. Zumalacárregui, Phys. Rev. Lett. **119,** 251304 (2017).

[64] V. Sahni and Y. Shtanov, J. Cosmol. Astropart. Phys. 11 (2003) 014.

[65] K. Koyama, Classical Quantum Gravity **24,** R231 (2007).

[66] F. Schmidt, Phys. Rev. D **80,** 043001 (2009).

[67] H. A. Winther and P. G. Ferreira, Phys. Rev. D **92,** 064005 (2015).

[68] B. Li, G.-B. Zhao, and K. Koyama, J. Cosmol. Astropart. Phys. 05 (2013) 023.

[69] T. P. Sotiriou, Classical Quantum Gravity **23,** 5117 (2006).

[70] S. Capozziello, E. de Filippis, and V. Salzano, Mon. Not. R. Astron. Soc. **394,** 947 (2009).

[71] V. Salzano, D. F. Mota, S. Capozziello, and N. R. Napolitano, Astron. Astrophys. **561,** A131 (2014).

[72] S. Capozziello, M. Faizal, M. Hameeda, B. Pourhassan, V. Salzano, and S. Upadhyay, Mon. Not. R. Astron. Soc. **474,** 2430 (2018).

[73] V. Salzano, D. F. Mota, S. Capozziello, and M. Donahue, Phys. Rev. D **95,** 044038 (2017).

[74] J. Khoury and A. Weltman, Phys. Rev. D **69,** 044026 (2004).

[75] S. Capozziello and S. Tsujikawa, Phys. Rev. D **77,** 107501 (2008).

[76] C. Burrage and J. Sakstein, J. Cosmol. Astropart. Phys. 11 (2016) 045.

[77] J. Sakstein and B. Jain, Phys. Rev. Lett. **119,** 251303 (2017).

[78] C. Burrage and J. Sakstein, Living Rev. Relativity **21,** 1 (2018).

[79] B. Li, G.-B. Zhao, R. Teyssier, and K. Koyama, J. Cosmol. Astropart. Phys. 01 (2012) 051.

[80] G. Hinshaw et al., Astrophys. J. Suppl. Ser. **208,** 19 (2013).

[81] A. J. Cuesta et al., Mon. Not. R. Astron. Soc. **457,** 1770 (2016).

[82] J. Richard et al., Messenger **175,** 50 (2019).

[83] W. A. Hellwing, B. Li, C. S. Frenk, and S. Cole, Mon. Not. R. Astron. Soc. **435,** 2806 (2013).

[84] M. Cataneo, D. Rapetti, L. Lombriser, and B. Li, J. Cosmol. Astropart. Phys. 12 (2016) 024.

[85] W. A. Hellwing, K. Koyama, B. Bose, and G.-B. Zhao, Phys. Rev. D **96,** 023515 (2017).

[86] N. C. Devi, A. Rodríguez-Puebla, O Valenzuela, V. Avila-Reese, C. Hernández-Aguayo, and B. Li, Mon. Not. R. Astron. Soc. **488,** 782 (2019).

[87] W. A. Hellwing, The skewness of $z = 0.5$ redshift-space galaxy distribution in Modified Gravity, in XXXIX Polish Astronomical Society Meeting, edited by K. Małek et al. (Polskie Towarzystwo Astronomiczne, Warsaw, Poland, 2020), Vol. 10, pp. 315–322.

[88] R. Liu, G. Valogiannis, N. Battaglia, and R. Bean, arXiv:2101.08728.

[89] https://bitbucket.org/gfcstanford/rockstar

[90] P. S. Behroozi, R. H. Wechsler, and H.-Y. Wu, Astrophys. J. **762,** 109 (2013).

[91] B. Li and H. Zhao, Phys. Rev. D **81,** 104047 (2010).https://bitbucket.org/gfcstanford/rockstar

[92] A. Aviles, K. Koyama, J. L. Cervantes-Cota, H. A. Winther, and B. Li, J. Cosmol. Astropart. Phys. 01 (2020) 006.

[93] F. Schmidt, A. Vikhlinin, and W. Hu, Phys. Rev. D **80,** 083505 (2009).

[94] A. A. Berlind, D. H. Weinberg, A. J. Benson, C. M. Baugh, S. Cole, R. Dave, C. S. Frenk, A. Jenkins, N. Katz, and C. G. Lacey, Astrophys. J. **593,** 1 (2003).

[95] Z. Zheng, A. A. Berlind, D. H. Weinberg, A. J. Benson, C. M. Baugh, S. Cole, R. Dave, C. S. Frenk, N. Katz, and C. G. Lacey, Astrophys. J. **633,** 791 (2005).

[96] Z. Zheng, A. L. Coil, and I. Zehavi, Astrophys. J. **667,** 760 (2007).

[97] M. Manera et al., Mon. Not. R. Astron. Soc. **428,** 1036 (2013).

[98] C. Hernández-Aguayo, C. M. Baugh, and B. Li, Mon. Not. R. Astron. Soc. **479,** 4824 (2018).

[99] E. Paillas, M. Cautun, B. Li, Y.-C. Cai, N. Padilla, J. Armijo, and S. Bose, Mon. Not. R. Astron. Soc. **484,** 1149 (2019).

[100] W. A. Hellwing, M. Schaller, C. S. Frenk, T. Theuns, J. Schaye, R. G. Bower, and R. A. Crain, Mon. Not. R. Astron. Soc. **461,** L11 (2016).

[101] F. Schmidt, Phys. Rev. D **81,** 103002 (2010).

[102] T. Y. Lam and B. Li, Mon. Not. R. Astron. Soc. **426,** 3260 (2012).

[103] L. Lombriser, B. Li, K. Koyama, and G.-B. Zhao, Phys. Rev. D **87,** 123511 (2013).

[104] A. Joyce, L. Lombriser, and F. Schmidt, Annu. Rev. Nucl. Part. Sci. **66,** 95 (2016).

[105] S. Hagstotz, M. Costanzi, M. Baldi, and J. Weller, Mon. Not. R. Astron. Soc. **486,** 3927 (2019).

[106] J. E. García-Farieta and R. Á. Casas-Miranda, *Massive Neutrinos and Galaxy Clustering in f(R) Gravity Cosmologies* (IntechOpen, London, 2020), pp. 195–214.

[107] J. Tinker, A. V. Kravtsov, A. Klypin, K. Abazajian, M. Warren, G. Yepes, S. Gottlöber, and D. E. Holz, Astrophys. J. **688,** 709 (2008).

[108] F. Schmidt, M. Lima, H. Oyaizu, and W. Hu, Phys. Rev. D **79,** 083518 (2009).

[109] F. Schmidt, Phys. Rev. D **80,** 123003 (2009).

[110] J. E. García-Farieta, F. Marulli, A. Veropalumbo, L. Moscardini, R. A. Casas-Miranda, C. Giocoli, and M. Baldi, Mon. Not. R. Astron. Soc. **488,** 1987 (2019).

[111] B. S. Wright, K. Koyama, H. A. Winther, and G.-B. Zhao, J. Cosmol. Astropart. Phys. 06 (2019) 040.

[112] E. A. Kazin et al., Astrophys. J. **710,** 1444 (2010).

[113] S. Alam et al., arXiv:2007.08991.

[114] D. Alonso, arXiv:1210.1833.

[115] S. D. Landy and A. S. Szalay, Astrophys. J. **412,** 64 (1993).

[116] A. J. S. Hamilton, Astrophys. J. **385,** L5 (1992).

[117] E. A. Kazin, A. G. Sánchez, and M. R. Blanton, Mon. Not. R. Astron. Soc. **419,** 3223 (2012).

[118] A. G. Sánchez et al., Mon. Not. R. Astron. Soc. **433,** 1202 (2013).

[119] A. J. S. Hamilton, Astrophys. J. **406,** L47 (1993).

[120] P. J. E. Peebles, *Principles of Physical Cosmology* (Princeton University Press, Princeton, NJ, 1993).

[121] L. Wang and P. J. Steinhardt, Astrophys. J. **508,** 483 (1998).

[122] A. Lue, R. Scoccimarro, and G. D. Starkman, Phys. Rev. D **69,** 124015 (2004).

[123] O. Lahav, P. B. Lilje, J. R. Primack, and M. J. Rees, Mon. Not. R. Astron. Soc. **251,** 128 (1991).

[124] E. V. Linder, Phys. Rev. D **72,** 043529 (2005).

[125] Y.-S. Song and W. J. Percival, J. Cosmol. Astropart. Phys. 10 (2009) 004.

[126] S. J. Hatton and S. Cole, Mon. Not. R. Astron. Soc. **296,** 10 (1998).

[127] T. Okumura and Y. P. Jing, Astrophys. J. **726,** 5 (2011).

[128] W. J. Percival, L. Samushia, A. J. Ross, C. Shapiro, and A. Raccanelli, Phil. Trans. R. Soc. A **369,** 5058 (2011).

[129] J.-H. He, L. Guzzo, B. Li, and C. M. Baugh, Nat. Astron. **2,** 967 (2018).

[130] P. Brax and P. Valageas, Phys. Rev. D **88,** 023527 (2013).

[131] L. Lombriser, F. Simpson, and A. Mead, Phys. Rev. Lett. **114,** 251101 (2015).

[132] R. E. Smith, R. Scoccimarro, and R. K. Sheth, Phys. Rev. D **75,** 063512 (2007).

[133] S. Basilakos and M. Plionis, Astrophys. J. **550,** 522 (2001).

[134] S. Basilakos, M. Plionis, and A. Pouri, Phys. Rev. D **83,** 123525 (2011).

[135] K. Hoffmann, J. Bel, and E. Gaztanaga, Mon. Not. R. Astron. Soc. **465,** 2225 (2017).

[136] P. M. Sutter, G. Lavaux, N. Hamaus, B. D. Wandelt, D. H. Weinberg, and M. S. Warren, Mon. Not. R. Astron. Soc. **442,** 462 (2014).

[137] T. Lazeyras, M. Musso, and F. Schmidt, J. Cosmol. Astropart. Phys. 03 (2017) 059.

[138] J. L. Tinker, B. E. Robertson, A. V. Kravtsov, A. Klypin, M. S. Warren, G. Yepes, and S. Gottlöber, Astrophys. J. **724,** 878 (2010).

[139] C. Alcock and B. Paczynski, Nature (London) **281,** 358 (1979).

[140] E. Hawkins et al., Mon. Not. R. Astron. Soc. **346,** 78 (2003).

[141] C. Adams and C. Blake, Mon. Not. R. Astron. Soc. **494,** 3275 (2020).

[142] A. Taruya, K. Koyama, and J. Soda, Astrophys. J. **510,** 541 (1999).

[143] T. Matsubara, Astrophys. J. **525,** 543 (1999).

[144] K. Yoshikawa, A. Taruya, Y. P. Jing, and Y. Suto, Astrophys. J. **558,** 520 (2001).

[145] M. Sato and T. Matsubara, Phys. Rev. D **87,** 123523 (2013).

[146] R. E. Smith, J. A. Peacock, A. Jenkins, S. D. M. White, C. S. Frenk, F. R. Pearce, P. A. Thomas, G. Efstathiou, and H. M. P. Couchman, Mon. Not. R. Astron. Soc. **341,** 1311 (2003).

[147] A. Lewis, A. Challinor, and A. Lasenby, Astrophys. J. **538,** 473 (2000).

[148] J. Lesgourgues, arXiv:1104.2932.

[149] B. A. Reid and M. White, Mon. Not. R. Astron. Soc. **417,** 1913 (2011).

[150] I. Achitouv, M. Baldi, E. Puchwein, and J. Weller, Phys. Rev. D **93,** 103522 (2016).

[151] N. Mirzatuny, S. Khosravi, S. Baghram, and H. Moshafi, J. Cosmol. Astropart. Phys. 01 (2014) 019.